White Rose Research Online

eprints@whiterose.ac.uk
https://eprints.whiterose.ac.uk
Universities of Leeds, Sheffield and York

Deposited via The University of Leeds.

White Rose Research Online URL for this paper:
https://eprints.whiterose.ac.uk/id/eprint/167236/

Version: Accepted Version

Article:
Crisóstomo-Figueroa, A, McArthur, AD, Dorrell, RM et al. (2021) A new modelling approach to sediment bypass prediction applied to the East Coast Basin, New Zealand. Geological Society of America Bulletin, 133 (7-8). pp. 1734-1748. ISSN: 0016-7606

https://doi.org/10.1130/B35687.1

© 2020 Geological Society of America. This is an author produced version of a journal article published in Geological Society of America Bulletin. Uploaded in accordance with the publisher's self-archiving policy.

Reuse
Items deposited in White Rose Research Online are protected by copyright, with all rights reserved unless indicated otherwise. They may be downloaded and/or printed for private study, or other acts as permitted by national copyright laws. The publisher or other rights holders may allow further reproduction and re-use of the full text version. This is indicated by the licence information on the White Rose Research Online record for the item.

Takedown
If you consider content in White Rose Research Online to be in breach of UK law, please notify us by emailing eprints@whiterose.ac.uk including the URL of the record and the reason for the withdrawal request.

A new modelling approach to sediment bypass prediction applied to the East Coast Basin, New Zealand

Adriana Crisóstomo-Figueroa[1], Adam D. McArthur[1], Robert M. Dorrell[2], Lawrence Amy[3], William D. McCaffrey[1]

[1] *Institute of Applied Geosciences, University of Leeds, Leeds, LS2 9JT, United Kingdom*

[2] *Energy and Environment Institute, University of Hull, Hull, HU6 7RX, United Kingdom*

[3] *School of Earth Sciences, University College Dublin, Belfield, Dublin 4, Ireland*

ABSTRACT

Predicting when turbidity currents are erosional or depositional (i.e., leaving no depositional record vs. leaving a deposit) remains challenging. Here we combined observations from submarine channel morphology with a new sediment transport model to derive thresholds for net erosional, equilibrium or net depositional flow and to predict how far turbidity currents can transport different grain size classes down-channel. The approach was applied to the modern Madden and Omakere channels, which traverse the Hikurangi subduction margin of the North Island of New Zealand. A bathymetric dataset was used to establish the downstream change of channel geometry. Taking account of centripetal and Coriolis forces, the flow superelevation method was used to estimate variations in flow velocity and concentration along the channels. These parameters were used as model inputs in order to estimate the potential distribution of sand in the system, assuming well sorted and poorly sorted sediment in suspension. The predicted sand distribution maps deposited by poorly sorted flows in the channels show good agreement with RMS amplitude mapping of the seafloor. These results confirm that thicker flows, and those carrying well sorted suspensions can bypass sediment over lower slopes than thinner flows and those carrying more poorly sorted suspensions. The net erosion and net deposition thresholds derived from this study may help to guide and constrain predictions of

potential sediment bypass zones in seafloor and subsurface systems, and hence better constrain the predicted *loci* of deposition.

INTRODUCTION

Deep-marine siliciclastic systems are volumetrically some of the most important sedimentary environments on the surface of the earth (Covault and Graham, 2010; Meiburg and Kneller, 2010; Talling et al., 2015). Submarine gravity currents (e.g. turbidity currents) transport sediment from shallow to deep-water, often developing complex depositional geometries (e.g. Richards and Bowman, 1998; Wynn et al., 2002; Booth et al., 2003; Gardner et al., 2003; Posamentier and Kolla, 2003; Deptuck et al., 2008; Ponce and Carmona, 2011; Dorrell et al., 2015; Spychala et al., 2017). Whether suspended sediment of a particular grain size is either transported up to the maximum flow runout distance, or deposited at any particular location along the flow pathway plays a key role in: 1) the distribution of sediment across shelf-to-basin slope profiles (Normark, 1978; Mutti and Normark, 1987; Prather et al., 1998; Wynn et al., 2002; Hadler-Jacobsen et al., 2005; Carvajal and Steel, 2009; Pyles et al., 2011); 2) the reservoir quality of turbidite sandstones through fractionation of different grain size classes (Pyles and Jennette, 2009; Horseman et al., 2014; Marchand et al., 2015; Bell et al., 2018); and 3) the development of up-dip stratigraphic pinch-outs that trap hydrocarbon reservoirs (Straccia and Prather, 2000; Carruth, 2003; Prather, 2003; Doré and Robbins, 2005; Milton-Worssell et al., 2006; Horseman et al., 2014; Van der Merwe et al., 2014; Amy, 2019; Hansen et al., 2019). However, determining whether a turbidity current transports or deposits sediment remains challenging, despite recent work observing and monitoring turbidity currents (Vangriesheim et al., 2009; Xu et al., 2014; Paull et al., 2018; Zhang et al., 2018).

Here we used a theoretical model for the threshold between net sediment erosion and net sediment deposition of turbidity currents to determine the grain sizes that might be

transported or deposited along the Madden and Omakere slope channels of the East Coast Basin (ECB), New Zealand. The submarine slope of the ECB represents an actively growing subduction wedge (Nicol et al., 2007; Barnes et al., 2010), with a series of trench-slope basins that are either supplied with sediment or starved, depending on the presence of slope channels (McArthur et al., 2019). The flow properties of turbidity currents were calculated based on an assumed relationship to the morphology of their confining channels. The thresholds between erosion and deposition were calculated assuming flows carrying non-cohesive sediment of a range of grain size classes and grain size distributions, accounting for the capacity and competence of the flow, flow height and bulk sediment concentration. Furthermore, the results from the model are validated by geophysical and petrophysical information. Here, we demonstrate that the grain size distribution in the flow has a large impact on sediment transport thresholds, therefore potentially controlling the sand distribution in the system.

Terminology

Despite its importance, there is no agreed definition of sediment bypass and bypassing flows between disciplines that study both associated sediment transport processes and products. In stratigraphic studies, *bypassing flow* or *bypass* have been broadly used for flows that partially or completely transport their sediment load beyond a point of observation (e.g. Lowe, 1982; Mutti and Normark, 1987; Amy et al., 2000; Cronin et al., 2005b; Kolla et al., 2007; Wynn et al., 2007; Carvajal and Steel, 2009; Talling et al., 2012; Stevenson et al., 2013; Sylvester et al., 2015). Furthermore, bypassing flow has also been used to refer to erosional flows despite the fundamental differences (i.e. changes in flow capacity) between both flow types (e.g. Mutti and Normark, 1987; Wynn et al., 2002; Hubbard et al., 2014; Stevenson et al., 2015; Lang et al., 2017). In contrast, previous experimental and numerical studies have defined non-depositional flows as equilibrium, self-sustaining or autosuspending flows (Bagnold, 1962; Kneller, 2003; Sequeiros et al., 2009; Dorrell et al., 2018). These definitions describe a flow

74 state where there is a net balance between sediment erosion and sediment deposition, and
75 allows differentiation of non-equilibrium flow regimes (i.e., erosional versus depositional
76 flow).

77 In an attempt to make a clear differentiation of bypassing flows in both process and
78 stratigraphic contexts, the terms *bypassing flows, partially bypassing flows* and *depositional*
79 *flows* have been suggested by Stevenson et al. (2015). These definitions provide a useful
80 framework in stratigraphic terms to distinguish flows that transport their complete load from
81 those that leave a deposit. However, in terms of process, the definition of depositional flows
82 implies that there must be some bypassing fraction in suspension, which overlaps with the
83 definition for partially bypassing flows. Therefore, for the purpose of this paper, we use the
84 following terminology which applies to the suspension load transported by channelized
85 turbidity currents (Fig. 1).

86 *Erosional flows* are non-equilibrium, under-capacity flows which entrain sediment into
87 suspension and transport it beyond the point of observation. *Equilibrium flows* are flows at
88 capacity, sediment deposition is balanced with erosion and allows for transport of their
89 complete suspension load beyond the point of observation, resulting in absence both of a
90 depositional record and of erosional features (e.g. Stevenson et al., 2013). *Depositional flows*
91 are non-equilibrium flows that are over capacity and deposit a fraction of their suspended load
92 whilst the remainder is further transported downstream. Here, s*ediment bypass* refers to the
93 process where sediment is transported beyond a point of observation by erosional flows,
94 equilibrium flows or depositional flows. The terms *deposition* and *bypass* preceded by the grain
95 size (e.g. sand deposition and silt bypass) will be used to differentiate the grain sizes that are
96 simultaneously deposited and bypassed at the point of observation.

97 **GEOLOGICAL SETTING**

98 The East Coast Basin (ECB) is a growing subduction wedge on and offshore of the eastern
99 margin of the North Island, New Zealand. The formation of the ECB is the result of collision
100 and oblique subduction of the Pacific Plate below the Australian Plate (Fig. 2) (Ballance, 1976;
101 Lewis and Bennett, 1985; Davey et al., 1986; Lewis and Pettinga, 1993; Nicol et al., 2007;
102 Bland et al., 2015; McArthur et al., 2019). The basin is limited to the east by the Hikurangi
103 subduction trench and to the west by the axial ranges of the North Island (Ballance, 1976;
104 Pettinga, 1982; Chanier and Ferriere, 1991; Nicol et al., 2007). The basin is dominated by NE-
105 SW striking thrust faulting, sub-parallel to the trench axis (Lewis and Pettinga, 1993) and is
106 divided into inner, mid and outer structural domains, each of which displays distinct
107 deformation styles (Fig. 2; McArthur et al., 2019).

108 Hikurangi Margin subduction initiated in the late Oligocene, at c. 25 Ma (Ballance,
109 1976; Chanier and Ferriere, 1991; Nicol et al., 2007; Reyners, 2013); this convergence has
110 created a series of elongate growth structures and trench-slope sub-basins, typically tens of
111 kilometers long by kilometers wide (Lewis and Pettinga, 1993; Barnes et al., 2010; Bailleul et
112 al., 2013; McArthur et al., 2019). Continued compression to the present day has resulted in
113 uplift and exhumation of the innermost trench-slope sub-basins, which are exposed at outcrop
114 (Bailleul et al., 2007), whilst the majority of the wedge remains submerged (Barnes et al.,
115 2010). Therefore, the basin predominantly experienced marine conditions during the Neogene,
116 with widespread deposition of mudstone and sandstone turbidites within bathymetric lows
117 (Bailleul et al., 2007; Burgreen-Chan et al., 2016), whilst submarine canyons and channels
118 incised ridges, acting as sediment conduits between sub-basins (McArthur and McCaffrey,
119 2019).

120 The present-day turbidite systems in the ECB dominantly transport very-fine sand and
121 silt (Barnes and Audru, 1999; Lewis and Pantin, 2002; Mountjoy et al., 2009; Wallace et al.,
122 2019). The sedimentation rates, character of sedimentary pathways and subsequent fill of sub-

basins varies throughout the subduction wedge, where a range of channels and submarine canyons are observed (Mountjoy et al., 2009; Bailleul et al., 2013; McArthur and McCaffrey, 2019). Channels in the northern and southern parts of the wedge potentially connect with the Hikurangi Channel (Fig. 2) (Mountjoy et al., 2009). Channels in the central zone terminate in the mid-portion of the wedge delivering sediment to mid and outer trench-slope sub-basins (McArthur and McCaffrey, 2019). This variation in sediment distribution systems has been interpreted to result partly from the development of high-angle thrust faults forming steeper ridges in the northern and southern zones of the basin (McArthur et al., 2019). Other sediment transport processes in the basin include debris flows (Mountjoy and Micallef, 2012; McArthur and McCaffrey, 2019) and contour currents (Carter et al., 1996, 2004; Bailey et al., 2020), together with hemipelagic fallout.

METHODS

Datasets and Morphological Analysis

Bathymetric data of the East Coast Basin with a horizontal resolution of 100 m (provided by the National Institute of Water and Atmospheric Research, New Zealand) were used to calculate the channel thalweg, and channel dimensions in the Madden and Omakere channels as illustrated in Figure 3. The calculations were conducted using the Topotoolbox program in MATLAB, which enables landscape and drainage analysis of digital elevation models (Schwanghart and Kuhn, 2010). The channel thalwegs were calculated from landscape drainage and the bathymetric profiles were used to calculate the thalweg down-slope gradient (S).

Channel dimensions were measured from channel cross-sectional profiles as represented in Figure 3. The cross-sections in each channel were taken perpendicular to the channel thalweg approximately every 2 km downstream. In levee-bound channel sections, the

147 mean channel height ($\overline{H}$) was calculated from the maximum (H) and minimum (h) levee crest
148 heights, which represent the relief between the channel thalweg and the channel flank top (Fig.
149 3). In sections where the channels were fully or partially ridge-confined, the erosional rim was
150 used as a proxy for flow height and for the calculation of H, h and $\overline{H}$ (Fig. 3). The maximum
151 channel width (W) represents the horizontal distance between the higher levee crest and the
152 lower levee crest, whereas the minimum channel width (w_m) is the horizontal distance between
153 the lower levee crest and the opposite channel wall. The mean channel width ($\overline{W}$) was
154 calculated from the maximum (W) and minimum (w_m) channel widths (Fig. 3). The width of
155 the channel floor (W_b) (Fig. 3) was measured perpendicular to the channel axis. The cross-
156 channel slope (γ) was calculated from the horizontal (W) and vertical difference (H-h) of the
157 levee crests or erosional rims, $\gamma = (H - h)/W$. The channel cross-sectional area (A) was
158 calculated using Eq. 1. The thalweg radius of curvature (r) (Fig. 3; cf. Keevil et al., 2007) was
159 measured at each channel bend.

160 $$A = \frac{W_b + W_m}{2} h + \frac{W_m}{2}(H - h). \quad (1)$$

161 The canyon-confined portion of the Madden Channel (Fig. 4) was omitted in the analysis
162 because estimates of the width and vertical channel relief do not permit estimation of flow
163 properties where traversing flows are unlikely to overtop the erosional confinement (see
164 below).

165 A 3D pre-stacked depth-migrated seismic dataset (acquired at broadband frequency in
166 2017) provided by WesternGeco Multiclient was used to map and generate the seafloor dip
167 map using Schlumberger's Petrel© E&P software (Fig. 5), and the root mean square (RMS)
168 amplitude map of the shallow subsurface (<50 m). The dataset has an inline (NW-SE) and
169 crossline (SW-NE) spacing of 25 m and a vertical resolution of 6.7 m. The vertical resolution
170 was approximated through the calculation of the tuning thickness (Widess, 1973), using a

171 wavenumber of $0.037\mathrm{m}^{-1}$ calculated from the instantaneous frequency attribute map of the
172 seafloor.

173 **Turbidity Current Modelling**

174 Downstream flow velocities and sediment concentration in the Madden and Omakere channels
175 were calculated using the cross-flow equation from Komar (1969), and the relationship
176 between the bed slope, densimetric Froude number and bed friction coefficient (Parker et al.
177 1987; Abad et al., 2011) that balances the gravitational force and drag force at the bed.

178 The cross-flow equation describes the balance of the Coriolis force, the centrifugal
179 force produced at channel bends and the pressure gradient in a turbidity current assuming a
180 bankfull flow (Komar, 1969), which can be used to reconstruct the flow properties of turbidity
181 currents (e.g. Bowen et al., 1984; Klaucke et al., 1997; Pirmez and Imran, 2003; Stevenson et
182 al., 2018). In clockwise flows in the Southern Hemisphere, the centrifugal and Coriolis forces
183 are oriented towards the outer bank, causing preferential overspill and cross-sectional channel
184 relief asymmetry, where the left-hand side bank is higher (looking in a downstream direction)
185 (Cossu and Wells, 2010; Dorrell et al., 2013a); whereas in anticlockwise flows, the forces are
186 opposed. At high latitudes, in straight channel sections, cross-sectional channel asymmetry
187 arises in the absence of centrifugal forces, due to Coriolis force alone (Cossu et al., 2010). The
188 cross-channel slope (γ in Fig. 3) is then used as a proxy of the superelevation of the boundary
189 between the flow and the ambient fluid (Komar, 1969).

190 The momentum balance of the pressure gradient force, the Coriolis force and the
191 centrifugal force across the channel (Komar, 1969; Stacey and Bowen, 1988; Wells and Cossu,
192 2013) can be written as,

193 $$gRC\gamma = \pm fU + \frac{U^2}{r}, \quad (2)$$

where g= 9.81 m/s^2 gravity; R=(ρ_s/ρ_f-1) is the excess density (where ρ_s=2650 kg/m^3 is the density of quartz for the material in suspension, and ρ_f=1030 kg/m^3 is the density of the fluid); C, the bulk sediment concentration (vol./vol.); $\gamma = (H - h)/W$, the cross-channel slope (m/m); f, the Coriolis acceleration f=2Ωsinθ, where -f for clockwise flows and +f for anticlockwise flows, Ω is the Earth's rotation rate, and θ the latitude (values for θ =-40.5° to -40.7° in the Madden Channel and -40.3° to -40.4° in the Omakere Channel); U, the downstream flow velocity in m/s; and r, the thalweg radius of curvature (m), in straight channel sections $r \to \infty$.

Eq. (2) can be rewritten in terms of the Froude number, Fr, (Cossu and Wells, 2010; Wells and Dorrell, 2020) where $Fr = U/\sqrt{gRC\overline{H}}$ (Parker et al. 1987),

$$\gamma = Fr^2\left(\frac{\pm f\overline{H}}{Fr\sqrt{gRC\overline{H}}} + \frac{\overline{H}}{r}\right), \quad (3)$$

where $\overline{H}$ is the mean flow depth (m).

Further, using the model of Parker et al. (1987) which balances gravitational driving force with frictional drag at the bed, and through the entrainment of ambient water (e.g. Abad et al. 2011),

$$S = \frac{Cd + e_w\left(1 + \frac{Ri}{2}\right)}{Ri}, \quad (4)$$

where S is the calculated down-channel slope in m/m; C_d=0.0025 (Abad et al., 2011; Konsoer et al., 2013), the drag coefficient, which is considered constant int the downstream direction for the calculated flows; Ri, the bulk Richardson number (which scales inversely with Fr^2 (Wells and Dorrell, 2020)) which is a measure of mixing of the flow-ambient fluid interface (Parker et al., 1987; Abad et al., 2011),

$$Ri = \frac{gRC\overline{H}}{U^2} = \frac{1}{Fr^2}, \quad (5)$$

and e_w, the ambient water entrainment by mixing is parameterized using

$$e_w = \frac{0.00153}{0.0204+Ri}, \quad (6)$$

a relation empirically derived by Parker et al., (1987) for turbidity currents.

A non-linear least squares MATLAB solver was used to derive *C* and *Fr* using Eqs. (3) to (6). *Fr* values were then used to calculate downstream flow velocities *U* in m/s using Eq. 7 (Parker et al., 1987; Abad et al., 2011). The shear velocity u^* was calculated in m/s via Eq. (8) (Parker et al., 1987; Abad et al., 2011); the flow discharge Q in m^3/s was calculated through Eq. (9) and sediment discharge Q_s in kg/s with Eq. (10) using the derived sediment concentration *C*:

$$U = Fr\sqrt{gRC\overline{H}}, \quad (7)$$

$$u^* = \sqrt{C_d}U, \quad (8)$$

$$Q = UA, \quad (9)$$

$$Qs = QC. \quad (10)$$

This analysis allows for improved estimations of bulk sediment concentrations for turbidity currents compared to previous work, where analyses do not jointly solve for Coriolis, gravitational and drag forces at straight channel sections and channel bends (Stevenson et al., 2018). The mean flow depth and bulk sediment concentration derived from this analysis were used as inputs into the sediment transport model to estimate the threshold between net sediment erosion and net deposition of turbidity currents.

Modelling of the Net Erosion and Net Deposition Threshold for Turbidity Currents

A Flow-Power Flux-Balance type model (Dorrell et al., 2018) was used to model the threshold of erosion and deposition for the turbidity current conditions estimated for the Madden and

Omakere channels. The model makes at-a-point predictions, and does not forward model the evolution of the currents nor the downdip transport of sediment in suspension (i.e. carried from source or eroded). In this analysis the average flow depths and sediment concentrations, calculated at each channel section from the cross-flow equation, were used to constrain the current hydrodynamics. The model incorporates the bulk capacity (maximum amount of sediment that can be transported in suspension by a turbulent flow), competence (particle class specific capacity) (Dorrell et al., 2013b), using a polydisperse description of sediment suspension. For each particle class the threshold between a net erosional and a depositional flow is given by

$$\frac{C_i^-}{C_m} E_i = C_i^+ w_{si} \forall i, \quad (11)$$

where the total concentration of sediments at the bed is

$$\sum_{i=1}^{N} c_i^- = c_m, \quad (12)$$

where C_i^- is the grain size class concentration in the active layer of the bed that freely exchanges material with material transported as suspended load (Dorrell et al., 2013b), C_m is the packing concentration , C_i^+ is the grain size class concentration at the bed and w_{si} the particle settling velocity for each grain size class. Further, the description of the vertical distribution of suspended sediment concentration was determined by the mass conservation equation

$$w_s C_i(Z) = -k_s \frac{dC_i(Z)}{dZ}, \quad (13)$$

where $Z = z/L$ is the dimensionless flow depth, $k_s = ku^* Lf(Z)$ is the eddy diffusivity which was assumed constant, therefore the flow length scale $L=h/6$, and the Rouse number is defined by $\beta = 6\frac{W_{si}}{ku_i^*}$ (Dorrell and Hogg, 2012), k=0.4 is the von Kármán constant; thus, the diffusion profile is given by

$$C_i(Z) = C_i^+ \left(\frac{1-e^{-\beta}}{\beta}\right). \quad (14)$$

The model incorporates a sediment entrainment function in which the power required to move sediment and incorporate it into suspension is proportional to the depth-averaged flow power:

$$E_i = \varepsilon\rho(gR\bar{H})^{-1}\Delta u_i^{*3}, \quad (15)$$

where $\varepsilon = 13.2$ (Dorrell et al., 2018) is an empirical parameter describing entrainment efficiency.

The characteristic grain size classes (d_{50}) used to solve Eq. (11) to Eq. (15) range from $\phi = 8$ to $\phi = -2$ (Wentworth scale; i.e., very fine silt to gravel). A log normal distribution derived from empirical data (Dorrell et al., 2018) was used to model grain size distribution, where a standard deviation $\sigma=0$ represents a monodisperse suspension, a standard deviation $\sigma = 0.5$ is equivalent to a polydisperse suspension that is well sorted (Folk, 1966) and a standard deviation $\sigma=2$ is equivalent to one that is poorly sorted (Folk, 1966). The slope gradient required to maintain equilibrium conditions for a given grain size and grain size distribution was calculated through Eq. (4) and presented in m/m and degrees. Then, the slope values in m/m calculated for each down-channel section were plotted in the net erosion-deposition threshold plots (Fig. 8 and Fig. 9).

RESULTS

Madden Canyon – Channel Morphology

The Madden Canyon is located downstream of the Madden Sub-basin where it incises the Madden Banks at water depths of ~1400 m. (Fig. 4). The Madden Canyon has been classified as being detached from direct hinterland supply (McArthur and McCaffrey, 2019). The canyon

head exhibits a funnel shape measuring ~9 km wide and exhibiting a V-shape morphology (Fig. 4A and Fig. 4B, cross section A1).

Given the changes in channel morphology and flow characteristics, the following division was established for the Madden Canyon - Channel:

1) The canyon-confined portion of the channel (not included in the turbidity current modelling, see methods) initiates from the Madden Banks breach-point (-1500 m water depth) to ~7 km downstream (-1800 m water depth) (Fig. 4A and Fig. 6A). A series of crescentic bedforms stepping basinward, and the steepest gradients of up to 3° are found in this section (Fig. 5).

2) The upper reaches of the channel (~35 km long) (cross section A2, Fig. 4B) comprise an area with an erosional terrace on the left bank (looking downstream), characterized by slide scars of mass failures from over steepened walls (Fig. 5), and a structurally confined levee on the right bank (Fig. 5B). Sediment waves migrating in a SSW direction perpendicular to the channel thalweg are present on the outer external levees (cf. Hansen et al., 2015) and terraces have formed likely due to the inward collapse of the external levees (inset in Fig. 5B). Knickpoints are observed in the canyon-confined portion as the channel crosses the axis of a tectonic fold and at the beginning of the upper reaches (Fig. 5B). The average channel height in the upper reaches is 380 m (Fig. 6B), the average channel width and area are 9.2 km and 1,899 km² respectively (Fig. 6C). Slope gradients in this section increase and decrease downstream, ranging from 2° to 0.04° (Fig. 6 A).

3) The Madden Channel - Porangahau section (~10 km long) comprises the area where the channel crosses the Porangahau Trough (cross-section A3, Fig. 4B). Sediment waves are observed on the outer external levees of the right bank, migrating in a SSW direction

perpendicular to the channel thalweg. On the left bank, sediment waves are also developed trending in a NNE direction. The levees have lower relief than those observed upstream in the upper reaches. Scours are present downstream on the channel floor (Fig. 5B). Channel heights (average channel height is 31 m), widths (average is 3.11 km) and area (57.7 km²) are lower compared to the channel upper reaches (Fig. 6B and Fig. 6B). Slope gradients are gentler, ranging from 0.02° to 0.04° (Fig. 6A).

4) The channel lower reaches (~20 km long) comprises the transect of the sub-basin between the Porangahau Ridge and the start of the Akitio Trough (cross section A4 and A5, Fig. 4B). In this area the channel is diverted by a growth ridge (cf. Clark and Cartwright, 2009), changing briefly to a trough-axial flow direction and limiting the left levee development (Fig. 5B). Sediment waves are developed in the outer right levee where the channel is diverted by the ridge structure (Fig. 5B). Then, the channel changes its course again, to resume a transverse orientation towards the Akitio Trough (Fig. 5B). The average channel height in this section is 16 m, average width of 1.31 km and area of 17.1 km^2 (Fig. 6B and Fig. 6C). The slope gradients in the lower reaches also has recurring steep slopes (2°, 1.2°) followed by more gentle slopes as in the upper reaches (Fig. 6A).

5) The Madden Channel terminates in the Akitio Trough which exhibits a uniform surface (cross section A6, Fig. 4B) with local emplacement of mass failure deposits (Fig. 5B). The lowest gradient of 0.01° is in this section (Fig. 6A).

Modelled Turbidity Current Conditions in the Madden Channel

The results from the turbidity current modelling in the Madden Channel are shown in Fig. 6. The flow velocity and shear velocity in the upper reaches of the channel show the highest values fluctuating from 8-12 m/s (Fig. 6D) and 0.4-0.6 m/s (Fig. 6F), respectively. A drop in

330 flow velocity to 3 m/s is observed at ~22 km decreasing gradually to 1.7 m/s in the last section
331 of the upper reaches, then to 0.7 m/s in the Porangahau section and finally there is an increase
332 up to 3.8 m/s in the lower reaches (Fig. 6D). The calculated velocities are within the ranges of
333 current velocities calculated from cable breaks and measured at submarine canyon systems
334 (0.02 m/s - 19 m/s) (Talling et al., 2013). *Fr* numbers from 2 to 1.2 downstream of the upper
335 reaches indicate super-critical flow conditions, which transition to sub-critical flow averaging
336 0.35. Flow deceleration and *Fr* values at this transition may indicate the development of an
337 internal hydraulic jump causing suspension and mixing near the bed which allows sediment
338 transport down-channel (Dorrell et al., 2016). The shear velocity decreases downstream to 0.15
339 m/s and 0.03 m/s in the upper reaches and Porangahau sections, respectively. Then, a slight
340 increase in flow velocity (up to 4 m/s) and shear velocity (up to 0.2 m/s) occurs at ~48 km
341 downstream in the lower reaches section. Supercritical flow conditions with Fr numbers from
342 1.9 to 1.6 prevail at the lower reaches as the channel passes through a steep area of structural
343 confinement.

344 The calculated bulk sediment concentrations exhibit less fluctuations in the upper
345 reaches and Porangahau sections with average values of 0.0074 v/v (0.7%) and 0.008 v/v
346 (0.8%) (Fig. 6G), respectively. A peak of 0.017 v/v (1.7%) occurs in the lower reaches at ~54
347 km downstream, the average sediment concentration in this section is of 0.009 v/v (0.9%). The
348 flow discharge and sediment discharge (Fig. 6H) display decreasing and increasing trends that
349 parallel those seen in the flow velocities and Froude number. The average flow discharge and
350 sediment discharge values in the upper reaches of the Madden Channel are 1.33×10^7 m^3/s and
351 1.04×10^8 kg/s, respectively. In the Porangahau section, the average values reduce to 5.25×10^4
352 m^3/s and 4.46×10^5 kg/s. The average flow discharge reduces to 5.14×10^4 m^3/s in the lower
353 reaches but the sediment discharge depicts an increment to 5.53×10^5 kg/s, reflecting the higher

354 sediment concentrations shown in the same section in Fig. 6G. These calculated flow
355 conditions allow us to investigate for erosion, equilibrium or deposition along the channel
356 profile.

357 **Sediment Bypass Conditions in the Madden Channel**

358 ***Well Sorted Flows***

359 The thresholds for equilibrium conditions of the modelled flows traversing each channel
360 section are shown from Fig. 8A to Fig. 8D. The contours represent the thresholds for well
361 sorted (σ=0.5), moderately sorted (σ=1) and poorly sorted (σ=2) sediment in suspension. For a
362 given slope value (*S*), the grain sizes (ϕ) above a given threshold represent sediment bypass
363 under erosional flow conditions and grain sizes below a given threshold represent deposition.
364 Note that the variation in particle size distribution (log-normal standard deviation), flow height
365 and down-slope channel gradient have an important effect on equilibrium.

366 The calculated flow of 380 m average height and 0.74% average sediment concentration
367 traversing the steep slopes (2°, 1.2°) in the upper reaches (Fig. 8A and Fig. 8E) can transport a
368 wider range of grain size classes (from very fine silt to medium sand) if they are suspended
369 within a well sorted flow (σ =0.5). However, for the same flow conditions and sorting, the
370 maximum grain size that can be maintained in suspension reduces to medium silt as the slope
371 gradients become gentler in the upper reaches (0.04°, 0.2°). As the flow reaches the Porangahau
372 section (Fig. 8B and Fig. 8E), the reduction in the average flow height to 31 m due to loss of
373 flow confinement in the Porangahau Trough, and gentle slopes of 0.04° causes a reduction of
374 the maximum grain size that can be transported in suspension to fine silt.

375 The steep slopes formed by the presence of the Porangahau Ridge at the start of the
376 channel lower reaches cause an increase in the driving force of the flow, consequently
377 increasing the flow velocity, shear velocity, bulk sediment concentration and discharge (Fig.

6). These changes in flow suggest that down-channel erosion might occur. Although the sediment being eroded depends on the composition of the bed, we can estimate that the maximum grain size class that can be transported in suspension is very fine sand, for the calculated flow conditions, assuming a well sorted flow travelling through the lower reaches (positions 6 and 7 in Fig. 8C and Fig. 8D, respectively). The channel terminates in the Akitio Trough where flows become unconfined.

Although the flow conditions in the Akitio Trough could not be calculated in the absence of channels, from the slope values in the trough (0.01°) it is estimated that most of the grain size classes would become depositional except for the very fine silt (position 8, Fig. 8D). Therefore, the maximum grain size that could be transported downstream by the modelled flows, from the upper reaches of the channel into the Akitio Trough, assuming a well sorted sediment in suspension, is very fine silt.

Poorly Sorted Flows

The equilibrium thresholds for poorly sorted suspensions ($\sigma = 2$) occur at higher slope values for all grain size classes compared to flows carrying well sorted suspensions ($\sigma = 0.5$). For the same flow conditions, the maximum grain size class that can be suspended in the flow and transported in the steep slopes (position 1, Fig. 8A and Fig. 8E) is very fine sand. However, it reduces to coarse silt (position 2, Fig. 8A and Fig. 8E), fine silt (position 3, Fig. 8A and Fig. 8E) and very fine silt (position 4, Fig. 8A and Fig. 8E) as the slope gradient decreases downstream.

As with the well sorted case, the equilibrium threshold for poorly sorted sediment in suspension in the Porangahau Trough suggest that all grain size classes would start to become depositional in this section (position 5, Fig. 8B), partly due to the low slope gradients and the

401 reduction in flow size. Slope gradients approximately above 0.1° would be required to keep the
402 very fine sand in suspension.

403 The increase in flow, shear velocities and sediment flux at the start of the channel lower
404 reaches suggest downstream erosion (Fig. 6). When poorly sorted material is eroded (assuming
405 this characterizes the composition of the substrate), we can estimate that the maximum grain
406 size that can be kept in suspension is medium silt throughout the lower reaches (positions 6 to
407 8, Fig. 8C and Fig. 8D). Any sand-size grains eroded would become depositional, limiting
408 further transport into the Akitio Trough (Fig. 8D).

409 **Omakere Channel Morphology**

410 A series of gullies incising the shelf at ~70 km offshore Hawke Bay constitute conduits that
411 feed the Omakere Channel (Fig. 2). The Omakere channel initiates as a trough axial channel in
412 the Omakere Trough at ~1500 m water depth. It evolves into a transverse channel traversing
413 troughs and eroding the Paoanui and Porangahau ridges and terminates in the Akitio Trough at
414 ~2270 m water depth (Fig. 4 and Fig. 7A).

415 The following division is established for the Omakere Channel given its changes in
416 morphology and flow characteristics:

417 1) The upper reaches of the Omakere Channel (~35 km long) initiate in the Omakere
418 Trough and is confined by thrust-faulted NE-SW oriented ridges (Fig. 4) which have
419 limited the development of levees. The channel exhibits a wide u-shape morphology in
420 the first ~25 km (cross-section B1, Fig 4C) which evolves to a box-shape at the end of
421 the upper reaches (cross-section B2, Fig.4C) likely due to down-channel tectonic
422 confinement. Therefore, the channel area decreases from 552 km² to 57 km².
423 Knickpoints developed in the most confined section (Fig. 5B) before the channel is
424 diverted into the upper reaches sub-basin. The average channel height in this section is

147 m, and average width of 3.96 km. There is a gentle slope of 0.09° followed by an increase up to 3° in the knickpoint area.

2) The Omakere Channel upper reaches sub-basin section (~15 km long) starts as the channel is diverted to a NW-SE direction by the Omakere Ridge (Fig. 4). The channel floor is smooth in this area. The average channel height decreases to 48 m due to loss of ridge-confinement as it enters the sub-basin and the average channel width increases to 6.14 km giving a wider U-shape morphology with subtle levee development (cross-section B3, Fig. 4C). The slope gradient in this area is gentler (0.12°) and less variable compared to the upper reaches.

3) The Omakere Channel-Paoanui section (~21 km long) starts where the channel course is diverted into the Paoanui Trough and subsequently cross-cuts the Paoanui Ridge. The channel widens in the trough giving a U-shape (cross-section B4, Fig. 4C) which narrows downslope as the channel height and ridge confinement increases (cross-section B5, Fig. 4C). The average channel height and area are 190 m and 783 $km^{2,}$ respectively. The slope gradient in this area increase with respect to the upper reaches sub-basin portion (Fig. 7A).

4) The lower reaches and the Akitio sections of the Omakere Channel (~15 km long) comprise the area where the channel cross-cuts the northern portion of the Porangahau ridge and other downstream ridges to terminate in the northern portion of the Akitio Trough. A series of knickpoints are observed at the start of the lower reaches where the slope gradient is steep (2°, Fig. 7A). The channel exhibits a box-shape as the channel widens due to loss of ridge confinement (cross-section B6, Fig. 4C) and subsequently becomes unconfined in the Akitio Trough (cross-section B7, Fig. 4C) where the slope decreases to 0.008° (Fig. 7A).

Modelled Turbidity Current Conditions in the Omakere Channel

450 The flow velocity in the Omakere Channel decreases from 3.2 m/s average in the upper reaches
451 to 1.8 m/s average velocity in the upper reaches sub-basin and increase downslope to 6.3 m/s
452 in the Paoanui Trough, then to 12 m/s average in the lower reaches and drops to 0.6 m/s in the
453 Akitio Trough (Fig. 7D). As in the Madden Channel, the calculated velocity values for the
454 Omakere Channel are within the ranges of current velocities observed at slope canyon systems
455 (0.02 m/s - 19 m/s) (Talling et al., 2013). The shear velocity exhibits an average value of 0.09
456 m/s at the upper reaches sub-basin and peaks at 0.8 m/s in the lower reaches, followed by a
457 decrease to 0.5 m/s as the flow reaches the Akitio Trough (Fig. 7D). The flow is predominantly
458 super-critical with phases of sub-critical flow at the start of the upper reaches and in the sub-
459 basin, where slope gradients are gentler (Fig. 7E).

460 The calculated bulk sediment concentration of the flow suggests more diluted flows at the
461 upper reaches with average values of 0.004 v/v (0.4%), which increase down-channel in the
462 Paoanui channel section and peaks at the lower reaches ~0.023 v/v (2.3%) (Fig. 7G). As with
463 the flow and shear velocities, the concentration drops in the Akitio Trough to ~0.003 v/v
464 (0.3%). The flow and sediment discharge initiate with an average of 1.51×10^6 m^3/s and
465 1.31×10^7 kg/s respectively in the upper reaches and increase down-channel to 3.98×10^6 m^3/s
466 and 7.87×10^7 kg/s (Fig. 7H).

467 **Sediment Bypass Conditions in the Omakere Channel**

468 ***Well Sorted Flows***

469 The thresholds for equilibrium conditions of the modelled flows traversing each channel
470 section are shown from Fig. 9A to Fig. 9D (see Well Sorted Flows section of the Madden
471 Channel on how to interpret the plots). The flow conditions calculated at the upper reaches
472 section, where slope gradients are gentle, show that the maximum grain size that can be kept
473 in suspension is coarse silt (0.09°, position 1, Fig. 9A). However, the maximum grain size

474 increases downstream over the steep slopes at ~25-31 km (positions 2, and 3, Fig. 9A) where
475 the erosional flows can transport up to fine sand.

476 The increase in sediment concentration suggests an erosional flow down-channel from
477 the upper reaches sub-basin (Fig. 9B) to the lower reaches (Fig. 9D), nevertheless, the different
478 grain sizes that can be suspended within such erosional flows varies at each channel section
479 due to the differences in flow height and variations in the slope gradient. As flows become less
480 confined and smaller in the upper reaches sub-basin, the thresholds widen and the maximum
481 grain size that can be maintained in suspension is coarse silt (position 4, Fig. 9B). The slope
482 gradient increases and maintains above 0.1° down-channel, flows increase in height in the
483 Paoanui Trough (positions 5 and 6, Fig. 9C) and the lower reaches (position 7, Fig. 9D),
484 therefore, the maximum grain size that can be suspended in these sections is fine sand.

485 As in the Madden Channel, the slope gradients in the Akitio Trough promote the
486 deposition of most grain size classes (position 8, Fig. 9D). Under well sorted conditions, the
487 maximum grain size that can be bypassed through the entire channel length and be deposited
488 in the Akitio Trough is coarse silt.

489 ***Poorly Sorted Flows***

490 The thresholds for equilibrium flow conditions assuming poorly sorted sediment in suspension
491 ($\sigma = 2$) show that the maximum grain size class that can be transported through the upper
492 reaches of the Omakere Channel is coarse silt (Fig. 9A) which reduces to very fine silt in the
493 upper reaches sub-basin (Fig. 9B). Nevertheless, flows evolving downstream could transport
494 larger grain sizes through erosional or equilibrium flows as they increase in height and
495 sediment concentration. In the Paoanui Trough, the maximum grain size that can be kept in
496 suspension is coarse silt (Fig. 9C) which increases to fine sand over the steep slopes in the

497 lower reaches (position 7, Fig. 9D). All grain sizes are calculated to be deposited as flows enter
498 the Akitio Trough (position 8, Fig. 9D).

499 **DISCUSSION**

500 **Controls on Sediment Bypass and Implications for Sand Distribution**

501 Results here suggest that in order to achieve very fine sand bypass (or coarser grain sizes)
502 through the ECB channels into outboard troughs, shallow flows (< 50 m) require steeper
503 gradients than thicker flows (> 140 m) under well sorted and poorly sorted conditions (Table
504 1). Furthermore, poorly sorted flows require steeper gradients than well sorted flows to achieve
505 very fine sand (or coarser) bypass, given that wider particle size distributions promote vertical
506 density stratification, hence, the magnitude of the shear stress in the flow must increase to
507 maintain sediment in suspension and reach equilibrium (Dorrell et al., 2018). Therefore, the
508 changes in the flow height, grain size distribution and slope gradient have an effect on the
509 equilibrium thresholds for sediment bypass and on the distribution of sand in the channels (Fig.
510 10).

511 Assuming a well sorted suspension of very fine sand and coarse silt, an equilibrium
512 flow develops in the upper reaches of the Madden Channel, enhanced by thick flows and steep
513 gradients. It may then become depositional as when reaching the Porangahau Trough, an area
514 of low confinement (hence the flow height reduces) and gentle slope gradients (Fig. 10A).
515 Therefore, very fine sand bypass into the lower reaches and Akitio Trough is limited and flows
516 rely on erosion to entrain very fine sand into suspension, if available, to continue sediment
517 transport downstream and deposit into the Akitio Trough (Fig. 10C). Similarly, the very fine
518 sand deposition in the Omakere Channel is more likely to occur in the Omakere Trough (upper
519 reaches section of the channel) where, although flows are more confined that in the Porangahau
520 section, it also constitutes an area of low gradient (Fig. 10A). As in the Madden Channel, flows

evolving downstream in the Omakere Channel must erode very fine sand in order to deposit it in the upper reaches sub-basin and Akitio Trough (Fig. 10C).

Assuming a poorly sorted suspension of very fine sand and very fine silt to medium silt, the wider grain size distribution promotes depositional flows with very fine sand deposition at the uppermost reaches of the Madden Channel and the Omakere Channel, and silt bypass down-channel (Fig. 10B). If erosional flows entrain very fine sand, the smaller magnitude of the flows combined with a poorly sorted suspension promote very fine sand deposition in the Madden and Omakere Channel sections as shown in Fig. 10D. Therefore, only the finer silt fraction bypasses to the Akitio Trough.

The results are compared to the RMS amplitude map of the seafloor (Fig. 10E), where high RMS amplitude responses indicative of high impedance contrast, are interpreted as sand-prone intervals, whereas low RMS amplitude responses indicate more homogeneous and finer-grained sediments. The high RMS amplitude patterns indicate sandier deposits along the Madden and Omakere channel thalweg (Fig. 10E), which are similar to the patterns projected for poorly sorted flows that erode sand down-channel (Fig. 10D). In the Madden Channel, higher RMS values along the channel thalweg are observed at the start of the upper reaches (Fig. 10F), and in the lower reaches (Fig. 10G) whereas low RMS values predominate in the Porangahau and Akitio Troughs. Furthermore, grain size analysis of drop cores in the Madden system have suggested poorly sorted deposits from very fine silt to fine sand (McKeown, 2018). Drop core M1 located in the upper reaches (Fig. 10E and 10F) was records a series of poorly sorted sediments, composed of interbedded very fine to coarse silt, silty fine sands and very fine sand beds (McKeown, 2018). Drop core M2 located in the Porangahau Trough (Fig. 10E and 10F) also consists of poorly sorted sediments, but only very fine to coarse silt beds were found here (McKeown, 2018). Sediments from drop core M3 located in the Akitio Trough (Fig. 10E and 10G) are poorly sorted, very fine to medium silt and sandy silt beds. Sediments

546 of M1 and M2 are in agreement with the deposits predicted from the model in the scenario
547 shown in Fig. 10D and the RMS amplitude map, suggesting these deposits might have been
548 the product of poorly sorted depositional flows with flow depths and bulk sediment
549 concentrations comparable with the modelling. Samples were not available from the Omakere
550 Channel, however RMS amplitude mapping can be used to examine our findings. Higher
551 amplitude values are located in the upper reaches (Fig. 10H), the Paoanui Trough (Fig. 10I)
552 and the lower reaches (Fig. 10I), whereas lower amplitude values predominate in the upper
553 reaches sub-basin and northern Akitio Trough, which shows good agreement with the patterns
554 projected for poorly sorted deposits in Fig. 10D. Differences in the distribution of sand in the
555 system might be due to other processes such as contour currents or bedload sediment transport
556 which are not considered in the modelling.

557 The results show that flows can change from sand bypass to deposition depending on
558 the characteristics of the turbidity current and that the bypass slope is not unique. Furthermore,
559 the thresholds derived from this study might help constrain the conditions required to develop
560 equilibrium flows over submarine slopes more generally. If a system has an up-dip slope of
561 0.25°, it would constitute a bypass slope for very fine sand when flows are approximately
562 thicker than 140 m (Table 1) whereas, for the same slope gradient and flow thickness, sand
563 would be deposited if poorly sorted conditions prevail as they would require slope gradients
564 above 0.8° to sustain bypass (Table 1). Thick flows (>140 m) with well sorted sediment in
565 suspension might aid the development of detached systems and possibly upslope pinch-outs,
566 when up-dip slopes are above 0.1°. Poorly sorted flows transporting sand might be depositional
567 throughout the feeder channel, hence, either promoting the formation of attached systems or
568 starved basins where only the finest grain sizes can be bypassed to the basin as observed in the
569 ECB (Fig. 10).

570 The thresholds are dependent on the assumptions made on the modelling, therefore the
571 thresholds for erosion, equilibrium and deposition might change for a different set of flow
572 height and sediment concentration. However, the thresholds derived from these flow conditions
573 might help guide and constrain interpretations of zones associated with equilibrium or
574 depositional flows in study areas where the slope gradient, the grain size and grain size
575 distribution are known such as in surface or subsurface deep-marine systems. Furthermore this
576 approach might allow us to predict areas of slope accommodation that may be starved or well
577 supplied with sands and thus help constrain and predict sediment distributions.

578 **CONCLUSIONS**

579 We calculated equilibrium thresholds to estimate sediment bypass in turbidity currents
580 traversing the Madden and Omakere channels of the East Coast Basin using the cross-flow
581 equation and Flow-Power Flux-Balance type model. This methodology allowed us to
582 determine that sediment bypass in the channels is controlled by changes in the flow height
583 (calculated from the channel morphology), by sediment sorting in the flow and by changes in
584 the seafloor gradient. On this basis, we derived maps for the potential distribution of very fine
585 sand, where deposits estimated from poorly sorted flows show good agreement with the
586 observations from the RMS amplitude map of the seafloor. The conditions required to achieve
587 sand bypass derived from this study might serve to screen other flow pathways of the East
588 Coast Basin and could be applied to other margins.

589 **ACKNOWLEDGEMENTS**

590 Thanks are given to CONACYT-SENER and the Turbidites Research Group sponsors
591 (AkerBP, CNOOC, ConocoPhillips, Murphy, OMV, and Oxy) for the funding of the research
592 project under which this work was undertaken. NIWA and WesternGeco Multiclient are also
593 thanked for providing the bathymetry and seismic datasets, respectively. We would also like to

thank the Associate Editor Rajat Mazumder, Ian R. Clark and two anonymous reviewers for their comments, and Editor Rob Strachan for handling the manuscript.

REFERENCES CITED

Abad, J.D., Sequeiros, O.E., Spinewine, B., Pirmez, C., Garcia, M.H., and Parker, G., 2011, Secondary Current of Saline Underflow In A Highly Meandering Channel: Experiments and Theory: Journal of Sedimentary Research, v. 81, p. 787–813, doi:10.2110/jsr.2011.61.

Amy, L.A., 2019, A review of producing fields inferred to have upslope stratigraphically trapped turbidite reservoirs: trapping styles (pure and combined), pinchout formation and depositional setting: American Association of Petroleum Geologists Bulletin, v. 103, p. 2861–2889, doi:10.1306/02251917408.

Amy, L., Kneller, B., and McCaffrey, W., 2000, Evaluating the Links Between Turbidite Characteristics and Gross System Architecture: Upscaling Insights from the Turbidite Sheet-System of Peïra Cava, SE France, *in* Weimer, P., Slatt, R.M., and Coleman, J. eds., Deep Water Reservoirs of the World: 20th Annual, Houston, TX, p. 1–15, doi:10.5724/gcs.00.15.0001.

Bagnold, R.A., 1962, Auto-suspension of transported sediment; turbidity currents: Proceedings of the Royal Society of London. Series A, Mathematical and Physical Sciences, v. 265, p. 315–319.

Bailey, W.S., McArthur, A.D., and McCaffrey, W.D., 2020, Distribution of contourite drifts on convergent margins: Examples from the Hikurangi subduction margin of New Zealand:, doi:10.1111/sed.12779.

Bailleul, J., Robin, C., Chanier, F., Guillocheau, F., Field, B., and Ferriere, J., 2007, Turbidite systems in the inner forearc domain of the Hikurangi convergent margin (New Zealand):

618 New constraints on the development of trench-slope basins: Journal of Sedimentary
619 Research, v. 77, p. 263–283, doi:10.2110/jsr.2007.028

620 Bailleul, J., Chanier, F., Ferrière, J., Robin, C., Nicol, A., Mahieux, G., Gorini, C., and Caron,
621 V., 2013, Neogene evolution of lower trench-slope basins and wedge development in the
622 central Hikurangi subduction margin, New Zealand: Tectonophysics, v. 591, p. 152–
623 174, doi:10.1016/j.tecto.2013.01.003.

624 Ballance, P.F., 1976, Evolution of the Upper Cenozoic Magmatic Arc and plate boundary in
625 northern New Zealand: Earth and Planetary Science Letters, v. 28, p. 356–370,
626 doi:10.1016/0012-821X(76)90197-7.

627 Barnes, P.M., and Audru, J.C., 1999, Quaternary faulting in the offshore Flaxbourne and
628 Wairarapa Basins, southern Cook Strait, New Zealand: New Zealand Journal of Geology
629 and Geophysics, v. 42, p. 349–367, doi:10.1080/00288306.1999.9514851.

630 Barnes, P.M., Lamarche, G., Bialas, J., Henrys, S., Pecher, I., Netzeband, G.L., Greinert, J.,
631 Mountjoy, J.J., Pedley, K., and Crutchley, G., 2010, Tectonic and geological framework
632 for gas hydrates and cold seeps on the Hikurangi subduction margin, New Zealand:
633 Marine Geology, v. 272, p. 26–48, doi:10.1016/j.margeo.2009.03.012.

634 Bell, D., Kane, I.A., Pontén, A.S.M., Flint, S.S., Hodgson, D.M., and Barrett, B.J., 2018,
635 Spatial variability in depositional reservoir quality of deep-water channel-fill and lobe
636 deposits: Marine and Petroleum Geology, v. 98, p. 97–115,
637 doi:10.1016/j.marpetgeo.2018.07.023.

638 Bland, K.J., Uruski, C.I., and Isaac, M.J., 2015, Pegasus Basin, eastern New Zealand: A
639 stratigraphic record of subsidence and subduction, ancient and modern: New Zealand
640 Journal of Geology and Geophysics, v. 58, p. 319–343,
641 doi:10.1080/00288306.2015.1076862.

642 Booth, J.R., Dean, M.C., DuVernay, A.E., and Styzen, M.J., 2003, Paleo-bathymetric
643 controls on the stratigraphic architecture and reservoir development of confined fans in
644 the Auger Basin: central Gulf of Mexico slope: Marine and Petroleum Geology, v. 20, p.
645 563–586, doi:10.1016/j.marpetgeo.2003.03.008.

646 Bowen, A.J., Normark, W.R., and Piper, D.J.W., 1984, Modelling of turbidity currents on
647 Navy Submarine Fan, California Continental Borderland: Sedimentology, v. 31, p. 169–
648 185, doi:10.1002/9781444304473.ch2.

649 Burgreen-Chan, B., Meisling, K.E., and Graham, S., 2016, Basin and petroleum system
650 modelling of the East Coast Basin, New Zealand: a test of overpressure scenarios in a
651 convergent margin: Basin Research, v. 28, p. 536–567, doi:10.1111/bre.12121.

652 Carruth, A.G., 2003, The Foinaven Field, Blocks 204/19 and 204/24a, UK North Sea:
653 Geological Society Memoir, v. 20, p. 121–130, doi:10.1144/GSL.MEM.2003.020.01.10.

654 Carter, R.M., Carter, L., and McCave, I.N., 1996, Current controlled sediment deposition
655 from the shelf to the deep ocean: The Cenozoic evolution of circulation through the SW
656 Pacific gateway: International Journal of Earth Sciences, v. 85, p. 438–451,
657 doi:10.1007/s005310050087.

658 Carter, L., Carter, R.M., and McCave, I.N., 2004, Evolution of the sedimentary system
659 beneath the deep Pacific inflow off eastern New Zealand: Marine Geology, v. 205, p. 9–
660 27, doi:10.1016/S0025-3227(04)00016-7.

661 Carvajal, C., and Steel, R., 2009, Shelf-edge architecture and bypass of sand to deep water:
662 Influence of shelf-edge processes, sea level, and sediment supply: Journal of
663 Sedimentary Research, v. 79, p. 652–672, doi:10.2110/jsr.2009.074.

664 Chanier, F., and Ferriere, J., 1991, From a passive to an active margin: tectonic and

665 sedimentary processes linked to the birth of an accretionary prism (Hikurangi margin,
666 New Zealand): Bulletin - Societe Geologique de France, v. 162, p. 649–660,
667 doi:10.2113/gssgfbull.162.4.649.

668 Clark, I.R., and Cartwright, J.A., 2009, Interactions between submarine channel systems and
669 deformation in deepwater fold belts: Examples from the Levant Basin, Eastern
670 Mediterranean sea: Marine and Petroleum Geology, v. 26, p. 1465–1482,
671 doi:10.1016/j.marpetgeo.2009.05.004.

672 Cossu, R., and Wells, M.G., 2010, Coriolis forces influence the secondary circulation of
673 gravity currents flowing in large-scale sinuous submarine channel systems: Geophysical
674 Research Letters, v. 37, p. 1–6, doi:10.1029/2010GL044296.

675 Cossu, R., Wells, M.G., and Whlin, A.K., 2010, Influence of the Coriolis force on the
676 velocity structure of gravity currents in straight submarine channel systems: Journal of
677 Geophysical Research, v. 115, p. 1–15, doi:10.1029/2010JC006208.

678 Covault, J.A., and Graham, S.A., 2010, Submarine fans at all sea-level stands: Tectono-
679 morphologic and climatic controls on terrigenous sediment delivery to the deep sea:
680 Geology, v. 38, p. 939–942, doi:10.1130/G31081.1.

681 Cronin, B.T., Çelik, H., Hurst, A., and Turkmen, I., 2005, Mud prone entrenched deep-water
682 slope channel complexes from the Eocene of eastern Turkey: Geological Society Special
683 Publication, v. 244, p. 155–180, doi:10.1144/GSL.SP.2005.244.01.10.

684 Davey, F.J., Hampton, M., Childs, J., Fisher, M.A., Lewis, K., and Pettinga, J.R., 1986,
685 Structure of a growing accretionary prism, Hikurangi margin, New Zealand.: Geology,
686 v. 14, p. 663–666.

687 Deptuck, M.E., Piper, D.J.W., Savoye, B., and Gervais, A., 2008, Dimensions and

688 architecture of late Pleistocene submarine lobes off the northern margin of East Corsica:
689 Sedimentology, v. 55, p. 869–898, doi:10.1111/j.1365-3091.2007.00926.x.

690 Doré, G., and Robbins, J., 2005, The Buzzard Field, *in* Petroleum Geology: North-West
691 Europe and Global Perspectives-Proceedings of the 6th Petroleum Geology Conference,
692 p. 241–252.

693 Dorrell, R.M., and Hogg, A.J., 2012, Length and Time Scales of Response of Sediment
694 Suspensions to Changing Flow Conditions: Journal of Hydraulic Engineering, v. 138, p.
695 430–439, doi:10.1061/(ASCE)HY.1943-7900.0000532.

696 Dorrell, R.M., Darby, S.E., Peakall, J., Sumner, E.J., Parsons, D.R., and Wynn, R.B., 2013a,
697 Superelevation and overspill control secondary flow dynamics in submarine channels:
698 Journal of Geophysical Research: Oceans, v. 118, p. 3895–3915,
699 doi:10.1002/jgrc.20277.

700 Dorrell, R.M., Hogg, A.J., and Pritchard, D., 2013b, Polydisperse suspensions: Erosion,
701 deposition, and flow capacity: Journal of Geophysical Research: Earth Surface, v. 118,
702 p. 1939–1955, doi:10.1002/jgrf.20129.

703 Dorrell, R.M., Burns, A.D., and McCaffrey, W.D., 2015, The inherent instability of leveed
704 seafloor channels: Geophysical Research Letters, v. 42, p. 4023–4031,
705 doi:10.1002/2015GL063809.

706 Dorrell, R.M., Peakall, J., Sumner, E.J., Parsons, D.R., Darby, S.E., Wynn, R.B., Özsoy, E.,
707 and Tezcan, D., 2016, Flow dynamics and mixing processes in hydraulic jump arrays:
708 Implications for channel-lobe transition zones: Marine Geology, v. 381, p. 181–193,
709 doi:10.1016/j.margeo.2016.09.009.

710 Dorrell, R.M., Amy, L.A., Peakall, J., and McCaffrey, W.D., 2018, Particle size distribution

711 controls the threshold between net sediment erosion and deposition in suspended load
712 dominated flows: Geophysical Research Letters, v. 45, p. 1443–1452,
713 doi:10.1002/2017GL076489.

714 Field, B.D., and Uruski, C.I., 1997, Cretaceous-Cenozoic geology and petroleum systems of
715 the East Coast region, New Zealand: Institute of Geological & Nuclear Sciences, v. 1.

716 Folk, R., 1966, A review of grain-size parameters: Sedimentology, v. 6, p. 73–93.

717 Gardner, M.H., Borer, J.M., Melick, J.J., Mavilla, N., Dechesne, M., and Wagerle, R.N.,
718 2003, Stratigraphic process-response model for submarine channels and related features
719 from studies of Permian Brushy Canyon outcrops, West Texas: Marine and Petroleum
720 Geology, v. 20, p. 757–787, doi:10.1016/j.marpetgeo.2003.07.004.

721 Hadler-Jacobsen, F., Johannessen, E.P., Ashton, N., Henriksen, S., Johnson, S.D., and
722 Kristensen, J.B., 2005, Submarine fan morphology and lithology distribution: A
723 predictable function of sediment delivery, gross shelf-to-basin relief, slope gradient and
724 basin topography, *in* Petroleum Geology: North-West Europe and Global Perspectives-
725 Proceedings of the 6th Petroleum Geology Conference, v. 6, p. 1121–1145,
726 doi:10.1144/0061121.

727 Hansen, L.A.S., Callow, R.H.T., Kane, I.A., Gamberi, F., Rovere, M., Cronin, B.T., and
728 Kneller, B.C., 2015, Genesis and character of thin-bedded turbidites associated with
729 submarine channels: Marine and Petroleum Geology, v. 67, p. 852–879,
730 doi:10.1016/j.marpetgeo.2015.06.007.

731 Hansen, L.A.S., Hodgson, D.M., Pontén, A., Bell, D., and Flint, S., 2019, Quantification of
732 basin-floor fan pinchouts: Examples from the Karoo Basin, South Africa: Frontiers in
733 Earth Science, v. 7, p. 1–20, doi:10.3389/feart.2019.00012.

734 Horseman, C., Ross, A., and Cannon, S., 2014, The discovery and appraisal of Glenlivet: A
735 West of Shetlands success story: Geological Society Special Publication, v. 397, p. 131–
736 144, doi:10.1144/SP397.10.

737 Hubbard, S.M., Covault, J.A., Fildani, A., and Romans, B.W., 2014, Sediment transfer and
738 deposition in slope channels: Deciphering the record of enigmatic deep-sea processes
739 from outcrop: Bulletin of the Geological Society of America, v. 126, p. 857–871,
740 doi:10.1130/B30996.1.

741 Keevil, G.M., Peakall, J., and Best, J.L., 2007, The influence of scale, slope and channel
742 geometry on the flow dynamics of submarine channels: Marine and Petroleum Geology,
743 v. 24, p. 487–503, doi:10.1016/j.marpetgeo.2007.01.009.

744 Klaucke, I., Hesse, R., and Ryan, W.B.F., 1997, Flow parameters of turbidity currents in a
745 low-sinuosity giant deep-sea channel: Sedimentology, v. 44, p. 1093–1102,
746 doi:10.1111/j.1365-3091.1997.tb02180.x.

747 Kneller, B., 2003, The influence of flow parameters on turbidite slope channel architecture:
748 Marine and Petroleum Geology, v. 20, p. 901–910,
749 doi:10.1016/j.marpetgeo.2003.03.001.

750 Kolla, V., Posamentier, H.W., and Wood, L.J., 2007, Deep-water and fluvial sinuous
751 channels-Characteristics, similarities and dissimilarities, and modes of formation:
752 Marine and Petroleum Geology, v. 24, p. 388–405,
753 doi:10.1016/j.marpetgeo.2007.01.007.

754 Komar, P.D., 1969, The channelized flow of turbidity currents with application to Monterey
755 deep-sea fan Channel: Journal of Geophysical Research, v. 74, p. 4544–4558.

756 Konsoer, K., Zinger, J., and Parker, G., 2013, Bankfull hydraulic geometry of submarine

channels created by turbidity currents: Relations between bankfull channel characteristics and formative flow discharge: Journal of Geophysical Research: Earth Surface, v. 118, p. 216–228, doi:10.1029/2012JF002422.

Lang, J., Brandes, C., and Winsemann, J., 2017, Erosion and deposition by supercritical density flows during channel avulsion and backfilling: Field examples from coarse-grained deepwater channel-levée complexes (Sandino Forearc Basin, southern Central America): Sedimentary Geology, v. 349, p. 79–102, doi:10.1016/j.sedgeo.2017.01.002.

Lewis, K.B., and Bennett, D.J., 1985, Structural patterns on the Hikurangi margin: an interpretation of new seismic data.:

Lewis, K.B., and Pantin, H.M., 2002, Channel-axis, overbank and drift sediment waves in the southern Hikurangi Trough, New Zealand: Marine Geology, v. 192, p. 123–151, doi:10.1016/S0025-3227(02)00552-2.

Lewis, K.B., and Pettinga, J.R., 1993, The emerging, imbricate frontal wedge of the Hikurangi margin: Sedimentary Basins of the World, v. 2, p. 225–250.

Lowe, D.R., 1982, Sediment gravity flows: II. Depositional models with special reference to the deposits of high-density turbidity currents.: Journal of Sedimentary Petrology, v. 52, p. 279–297.

Marchand, A.M.E., Apps, G., Li, W., and Rotzien, J.R., 2015, Depositional processes and impact on reservoir quality in deepwater Paleogene reservoirs, US Gulf of Mexico: American Association of Petroleum Geologists Bulletin, v. 99, p. 1635–1648, doi:10.1306/04091514189.

McArthur, A.D., and McCaffrey, W.D., 2019, Sedimentary architecture of detached deep-marine canyons: Examples from the East Coast Basin of New Zealand: Sedimentology,

v. 66, p. 1067–1101, doi:10.1111/sed.12536.

McArthur, A.D., Claussmann, B., Bailleul, J., Clare, A., and McCaffrey, W.D., 2019, Variation in syn-subduction sedimentation patterns from inner to outer portions of deep-water fold and thrust belts: examples from the Hikurangi subduction margin of New Zealand: Geological Society, London, Special Publications, v. 490, doi:10.1144/sp490-2018-95.

McKeown, M.C., 2018, Understanding the physical sedimentology of the modern Madden Canyon distributary system, New Zealand: University of Auckland, 1–135 p.

Meiburg, E., and Kneller, B., 2010, Turbidity Currents and Their Deposits: Annual Review of Fluid Mechanics, v. 42, p. 135–156, doi:10.1146/annurev-fluid-121108-145618.

Milton-Worssell, R.J., Stoker, S.J., and Cavill, J.E., 2006, Lower Cretaceous deep-water sandstone plays in the UK Central Graben: Geological Society Special Publication, v. 254, p. 169–186, doi:10.1144/GSL.SP.2006.254.01.09.

Mountjoy, J.J., and Micallef, A., 2012, Polyphase emplacement of a 30 km^3 blocky debris avalanche and its role in slope-gully development, *in* Submarine mass movements and their consequences, p. 213–222.

Mountjoy, J.J., Barnes, P.M., and Pettinga, J.R., 2009, Morphostructure and evolution of submarine canyons across an active margin: Cook Strait sector of the Hikurangi Margin, New Zealand: Marine Geology, v. 260, p. 45–68, doi:10.1016/j.margeo.2009.01.006.

Mutti, E., and Normark, W.R., 1987, Comparing examples of modern and ancient turbidite systems: problems and concepts, *in* Marine Clastic Sedimentology: Concepts and case studies, p. 1–38, doi:10.1007/978-94-009-3241-8_1.

Nicol, A., Mazengarb, C., Chanier, F., Rait, G., Uruski, C., and Wallace, L., 2007, Tectonic

803 evolution of the active Hikurangi subduction margin, New Zealand, since the Oligocene:
804 Tectonics, v. 26, p. 1–24, doi:10.1029/2006TC002090.

805 Normark, W.R., 1978, Fan valleys, channels, and depositional lobes on modern submarine
806 fans: characters for recognition of sandy turbidite environments: American Association
807 of Petroleum Geologists Bulletin, v. 62, p. 912–931, doi:10.1306/c1ea4f72-16c9-11d7-
808 8645000102c1865d.

809 Parker, G., 1982, Conditions for the ignition of catastrophically erosive turbidity currents:
810 Marine Geology, v. 46, p. 307–327.

811 Parker, G., Fukushima, Y., and Pantin, H., 1986, Self-accelerating turbidity currents: Journal
812 of Fluid Mechanics, v. 171, p. 145–181, doi:10.1017/S0022112086001404.

813 Parker, G., Garcia, M., Fukushima, Y., and Yu, W., 1987, Experiments on turbidity currents
814 over an erodible bed: Journal of Hydraulic Research, v. 25, p. 123–147,
815 doi:10.1080/00221688709499292.

816 Paull, C.K. et al., 2018, Powerful turbidity currents driven by dense basal layers: Nature
817 Communications, v. 9, p. 1–9, doi:10.1038/s41467-018-06254-6.

818 Pettinga, J.R., 1982, Upper cenozoic structural history, coastal southern Hawke's Bay, New
819 Zealand: New Zealand Journal of Geology and Geophysics, v. 25, p. 149–191,
820 doi:10.1080/00288306.1982.10421407.

821 Pirmez, C., and Imran, J., 2003, Reconstruction of turbidity currents in Amazon Channel:
822 Marine and Petroleum Geology, v. 20, p. 823–849,
823 doi:10.1016/j.marpetgeo.2003.03.005.

824 Ponce, J.J., and Carmona, N.B., 2011, Miocene deep-marine hyperpycnal channel levee
825 complexes, Tierra del Fuego, Argentina: Facies associations and architectural elements,

826 *in* Slatt, R.M. and Zavala, C. eds., Sediment transfer from shelf to deep water—
827 Revisiting the delivery system, The American Association of Petroleum Geologists, p.
828 75–93, doi:10.1306/13271351St613439.

829 Posamentier, H.W., and Kolla, V., 2003, Seismic geomorphology and stratigraphy of
830 depositional elements in deep-water settings: Journal of Sedimentary Research, v. 73, p.
831 367–388, doi:10.1306/111302730367.

832 Prather, B.E., 2003, Controls on reservoir distribution, architecture and stratigraphic trapping
833 in slope settings: Marine and Petroleum Geology, v. 20, p. 529–545,
834 doi:10.1016/j.marpetgeo.2003.03.009.

835 Prather, B.E., Booth, J.R., Steffens, G.S., and Craig, P.A., 1998, Classification, lithologic
836 calibration, and stratigraphic succession of seismic facies of intraslope basins, deep-
837 water Gulf of Mexico: The American Association of Petroleum Geologists Bulletin, v.
838 82, p. 701–728.

839 Pyles, D.R., and Jennette, D.C., 2009, Geometry and architectural associations of co-genetic
840 debrite-turbidite beds in basin-margin strata, Carboniferous Ross Sandstone (Ireland):
841 Applications to reservoirs located on the margins of structurally confined submarine
842 fans: Marine and Petroleum Geology, v. 26, p. 1974–1996,
843 doi:10.1016/j.marpetgeo.2009.02.018.

844 Pyles, D.R., Syvitski, J.P.M., and Slatt, R.M., 2011, Defining the concept of stratigraphic
845 grade and applying it to stratal (reservoir) architecture and evolution of the slope-to-
846 basin profile: An outcrop perspective: Marine and Petroleum Geology, v. 28, p. 675–
847 697, doi:10.1016/j.marpetgeo.2010.07.006.

848 Reyners, M., 2013, The central role of the Hikurangi Plateau in the Cenozoic tectonics of
849 New Zealand and the Southwest Pacific: Earth and Planetary Science Letters, v. 361, p.

460–468, doi:10.1016/j.epsl.2012.11.010.

Richards, M., and Bowman, M., 1998, Submarine fans and related depositional systems II: Variability in reservoir architecture and wireline log character: Marine and Petroleum Geology, v. 15, p. 821–839, doi:10.1016/S0264-8172(98)00042-7.

Schwanghart, W., and Kuhn, N.J., 2010, TopoToolbox: A set of Matlab functions for topographic analysis: Environmental Modelling and Software, v. 25, p. 770–781, doi:10.1016/j.envsoft.2009.12.002.

Sequeiros, O.E., Naruse, H., Endo, N., Garcia, M.H., and Parker, G., 2009, Experimental study on self-accelerating turbidity currents: Journal of Geophysical Research: Oceans, v. 114, p. 1–26, doi:10.1029/2008JC005149.

Spychala, Y.T., Hodgson, D.M., Prélat, A., Kane, I.A., Flint, S.S., and Mountney, N.P., 2017, Frontal and lateral submarine lobe fringes: Comparing sedimentary facies, architecture and flow processes: Journal of Sedimentary Research, v. 87, p. 75–96, doi:10.2110/jsr.2017.2.

Stacey, M.W., and Bowen, A.J., 1988, The vertical structure of density and turbidity currents: theory and observations: Journal of Geophysical Research, v. 93, p. 3528–3542, doi:10.1029/JC093iC04p03528.

Stevenson, C.J., Talling, P.J., Wynn, R.B., Masson, D.G., Hunt, J.E., Frenz, M., Akhmetzhanhov, A., and Cronin, B.T., 2013, The flows that left no trace: Very large-volume turbidity currents that bypassed sediment through submarine channels without eroding the sea floor: Marine and Petroleum Geology, v. 41, p. 186–205, doi:10.1016/j.marpetgeo.2012.02.008.

Stevenson, C.J., Jackson, C.A.-L., Hodgson, D.M., Hubbard, S.M., and Eggenhuisen, J.T.,

873 2015, Deep-Water Sediment Bypass: Journal of Sedimentary Research, v. 85, p. 1058–
874 1081, doi:10.2110/jsr.2015.63.

875 Stevenson, C.J., Feldens, P., Georgiopoulou, A., Schönke, M., Krastel, S., Piper, D.J.W.,
876 Lindhorst, K., and Mosher, D., 2018, Reconstructing the sediment concentration of a
877 giant submarine gravity flow: Nature Communications, v. 9, p. 1–7,
878 doi:10.1038/s41467-018-05042-6.

879 Straccia, J.R., and Prather, B.E., 2000, Stratigraphic traps in deep-water turbidite reservoirs at
880 the base of depositional slope, *in* Proceedings from the 2000 American Association of
881 Petroleum Geologists Annual Meeting,.

882 Sylvester, Z., Cantelli, A., and Pirmez, C., 2015, Stratigraphic evolution of intraslope
883 minibasins: Insights from surface-based model: American Association of Petroleum
884 Geologists BulletinAPG Bulletin, v. 99, p. 1099–1129, doi:10.1306/01081514082.

885 Talling, P.J., Masson, D.G., Sumner, E.J., and Malgesini, G., 2012, Subaqueous sediment
886 density flows: Depositional processes and deposit types: Sedimentology, v. 59, p. 1937–
887 2003, doi:10.1111/j.1365-3091.2012.01353.x.

888 Talling, P.J., Paull, C.K., and Piper, D.J.W., 2013, How are subaqueous sediment density
889 flows triggered, what is their internal structure and how does it evolve? Direct
890 observations from monitoring of active flows: Earth-Science Reviews, v. 125, p. 244–
891 287, doi:10.1016/j.earscirev.2013.07.005.

892 Talling, P.J. et al., 2015, Key future directions for research on turbidity currents and their
893 deposits: Journal of Sedimentary Research, v. 85, p. 153–169, doi:10.2110/jsr.2015.03.

894 Van der Merwe, W.C., Hodgson, D.M., Brunt, R.L., and Flint, S.S., 2014, Depositional
895 architecture of sand-attached and sand-detached channel-lobe transition zones on an

exhumed stepped slope mapped over a 2500 km2 area: Geosphere, v. 10, p. 1076–1093, doi:10.1130/GES01035.1.

Vangriesheim, A., Khripounoff, A., and Crassous, P., 2009, Turbidity events observed in situ along the Congo submarine channel: Deep-Sea Research Part II: Topical Studies in Oceanography, doi:10.1016/j.dsr2.2009.04.004.

Wallace, L.M., Saffer, D.M., Barnes, P.M., Pecher, I.A., Petronotis, K.E. LeVay, L.., and Expedition 372/375 Scientists, 2019, Hikurangi Subduction Margin Coring, Logging, and Observatories: Proceedings of the International Ocean Discovery Program, v. 372B/375, doi:https://doi.org/10.14379/iodp.proc.372B375.2019.

Wells, M., and Cossu, R., 2013, The possible role of Coriolis forces in structuring large-scale sinuous patterns of submarine channel – levee systems: Philosophical transactions of the Royal Society A, v. 371, p. 20120366.

Wells, M.G., and Dorrell, R.M., 2020, Turbulence processes within Turbidity Currents: Annual Review of Fluid Mechanics, v. 53, p. 59–83, doi:https://doi.org/10.1146/annurev-fluid-010719- 060309.

Widess, M.B., 1973, How thin is a thin bed? Geophysics, v. 38, p. 1176–1180.

Wynn, R.B., Kenyon, N.H., Masson, D.G., Stow, D.A.V., and Weaver, P.P.E., 2002, Characterization and recognition of deep-water channel-lobe transition zones: American Association of Petroleum Geologists BulletinAPG Bulletin, v. 86, p. 1441–1462.

Wynn, R.B., Cronin, B.T., and Peakall, J., 2007, Sinuous deep-water channels: Genesis, geometry and architecture: Marine and Petroleum Geology, v. 24, p. 341–387, doi:10.1016/j.marpetgeo.2007.06.001.

Xu, J.P., Sequeiros, O.E., and Noble, M.A., 2014, Sediment concentrations, flow conditions,

and downstream evolution of two turbidity currents, Monterey Canyon, USA: Deep-Sea Research Part I: Oceanographic Research Papers, v. 89, p. 11–34, doi:10.1016/j.dsr.2014.04.001.

Zhang, Y., Liu, Z., Zhao, Y., Colin, C., Zhang, X., Wang, M., Zhao, S., and Kneller, B., 2018, Long-term in situ observations on typhoon-triggered turbidity currents in the deep sea: Geology, v. 46, p. 675–678, doi:10.1130/G45178.1.

FIGURE CAPTIONS

Figure 1. Process terminology used in this study for a channelized turbidity current.

Figure 2. Study area. (A) The East Coast Basin is located on and offshore of the North Island, New Zealand and is limited to the east by the Hikurangi Trough and to the west by the axial ranges. (B) Offshore bathymetry map and bathymetric contours (500 m) of the East Coast Basin (courtesy of the National Institute of Water and Atmospheric Research, New Zealand). (C) Regional cross-section across the Hikurangi subduction complex (after Nicol et al., 2007).

Figure 3. Diagram showing the morphometric parameters measured at channel bends, levee-bound channel cross-sections and erosional channel cross-sections of the Madden and Omakere channels.

Figure 4. (A) The bathymetry map and bathymetric contours (500 m) courtesy of NIWA, show the Madden Channel and Omakere Channel systems. The channel thalweg line styles differentiate the sub-channel sections described in this study. (B) Selected cross-sectional profiles (with orientation looking downstream) of the Madden Channel highlighting the down-channel evolution from the canyon-confined portion (transect A1) to the Akitio Trough (transect A6). Transect location shown in A. (C) Selected cross-sectional profiles of the

942 Omakere Channel from the channel upper reaches (transect B1) to the northern Akitio
943 Trough (transect B7).

944 Figure 5. (A) Seafloor dip map of the Madden and Omakere channels derived from 3D
945 seismic data provided by WesternGeco Multiclient. (B) Interpreted seafloor dip map
946 showing morphological features of the channels resulted from tectonic and sedimentary
947 processes. The interpretation of the crests of thrust-faulted bathymetric ridges is derived from
948 Barnes et al. (2010).

949 Figure 6. Calculated dimensions and turbidity current conditions in the Madden Channel
950 from the upper reaches through the lower reaches section (sub-sections of the channel are
951 shown at the top of the plots). (A) Channel thalweg depth profile (solid line) and slope
952 gradient profile (dotted line) with values presented in degrees. (B) Average channel height
953 profile (solid line) and cross-channel slope values (triangles). (C) Average channel width
954 (solid line) and channel area (crosses). (D) Downstream turbidity current velocity profile. (E)
955 Froude number profile, dashed line at 1 indicates the threshold between sub-critical and
956 super-critical flow. Downstream (F) shear velocity, (G) bulk sediment concentration, (H)
957 flow discharge and sediment discharge profiles.

958 Figure 7. Calculated dimensions and turbidity current conditions in the Omakere Channel
959 from the upper reaches through the Akitio Trough section (sub-sections of the channel are
960 shown at the top of the plots). (A) Channel thalweg depth profile (solid line) and slope
961 gradient profile (dotted line) with values presented in degrees. (B) Average channel height
962 profile (solid line) and cross-channel slope values (triangles). (C) Average channel width
963 (solid line) and channel area (crosses). (D) Downstream turbidity current velocity profile. (E)
964 Froude number profile, dashed line at 1 indicates the threshold between sub-critical and

965 super-critical flow. Downstream (F) shear velocity, (G) bulk sediment concentration, (H)
966 flow discharge and sediment discharge profiles.

967 Figure 8. Plots showing the thresholds of equilibrium flow for the modelled turbidity current
968 traversing each section of the Madden Channel. The thresholds vary from well sorted (σ=0.5)
969 to poorly sorted (σ=2) sediment in suspension. For a given slope value (S), the grain sizes (ϕ)
970 above a given threshold represent sediment bypass under erosional flow conditions and grain
971 sizes below a given threshold represent deposition. The average flow height, $\overline{H}$, and average
972 bulk sediment concentration, C, used for the calculation of the thresholds are shown in each
973 plot for the (A) channel upper reaches (B) Porangahau Trough, (C) channel lower reaches
974 and (D) channel lower reaches and Akitio Trough. (E) Channel thalweg depth profile. The
975 numbers in black squares show the positions of the slope gradient values plotted in A-D.

976 Figure 9. Plots showing the thresholds of equilibrium flow for the modelled turbidity current
977 traversing the Omakere Channel. The thresholds vary from well sorted (σ=0.5) to poorly sorted
978 (σ=2) sediment in suspension. For a given slope value (S), the grain sizes (ϕ) above a given
979 threshold represent sediment bypass under erosional flow conditions and grain sizes below a
980 given threshold represent deposition. The average flow height, $\overline{H}$, and average bulk sediment
981 concentration, C, used for the calculation of the thresholds are shown in each plot for the (A)
982 channel upper reaches (B) upper reaches sub-basin, (C) Paoanui Trough and (D) channel lower
983 reaches and Akitio Trough. (E) Channel thalweg depth profile. The numbers in black squares
984 show the positions of the slope gradient values plotted in A-D.

985 Figure 10. (A-D) Potential sand distribution maps of the Madden and Omakere Channel
986 systems. The maps show the deposition from (A) a well sorted turbidity current transporting
987 very fine sand; (B) a poorly sorted turbidity current transporting very fine sand and very fine
988 sand to medium silt; (C) a well sorted turbidity current transporting very fine sand and coarse

silt, assuming downstream erosion of sand; (D) a poorly sorted turbidity current transporting very fine sand and very fine sand to medium silt assuming downstream erosion of sand. (E) Root Mean Square (RMS) amplitude map of the seafloor with drop core locations M1-M3. High RMS amplitude values are interpreted to represent deposits with higher sand content. Low RMS amplitude responses are interpreted to represent soft homogeneous finer-grained deposits. Enlarged areas showing the RMS amplitude distribution of the (F) Madden Channel upper reaches and Porangahau sections, (G) Madden Channel lower reaches, (H) Omakere upper reaches and (I) Omakere Channel Paoanui and lower reaches sections.

FIGURE 1

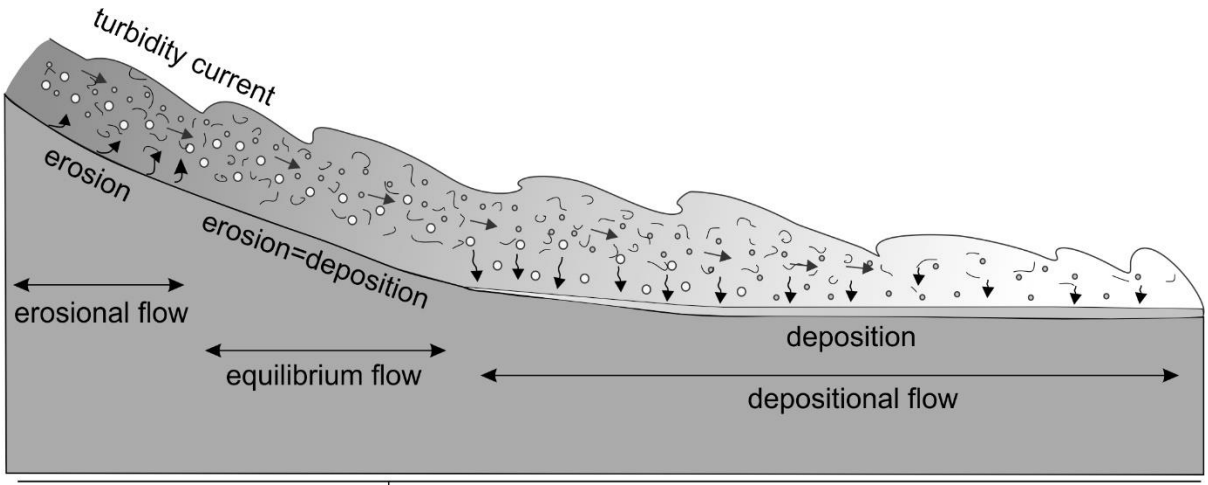

Process term	Definition
Erosional flow	A flow that erodes the substrate and entrains sediment into suspension, which might result in the development of erosional features.
Equilibrium flow	A flow where erosion is balanced with deposition, and transports its complete suspension load beyond the point of observation.
Depositional flow	A flow that deposits part of its suspension load and transports the remainder load downstream.

FIGURE 2

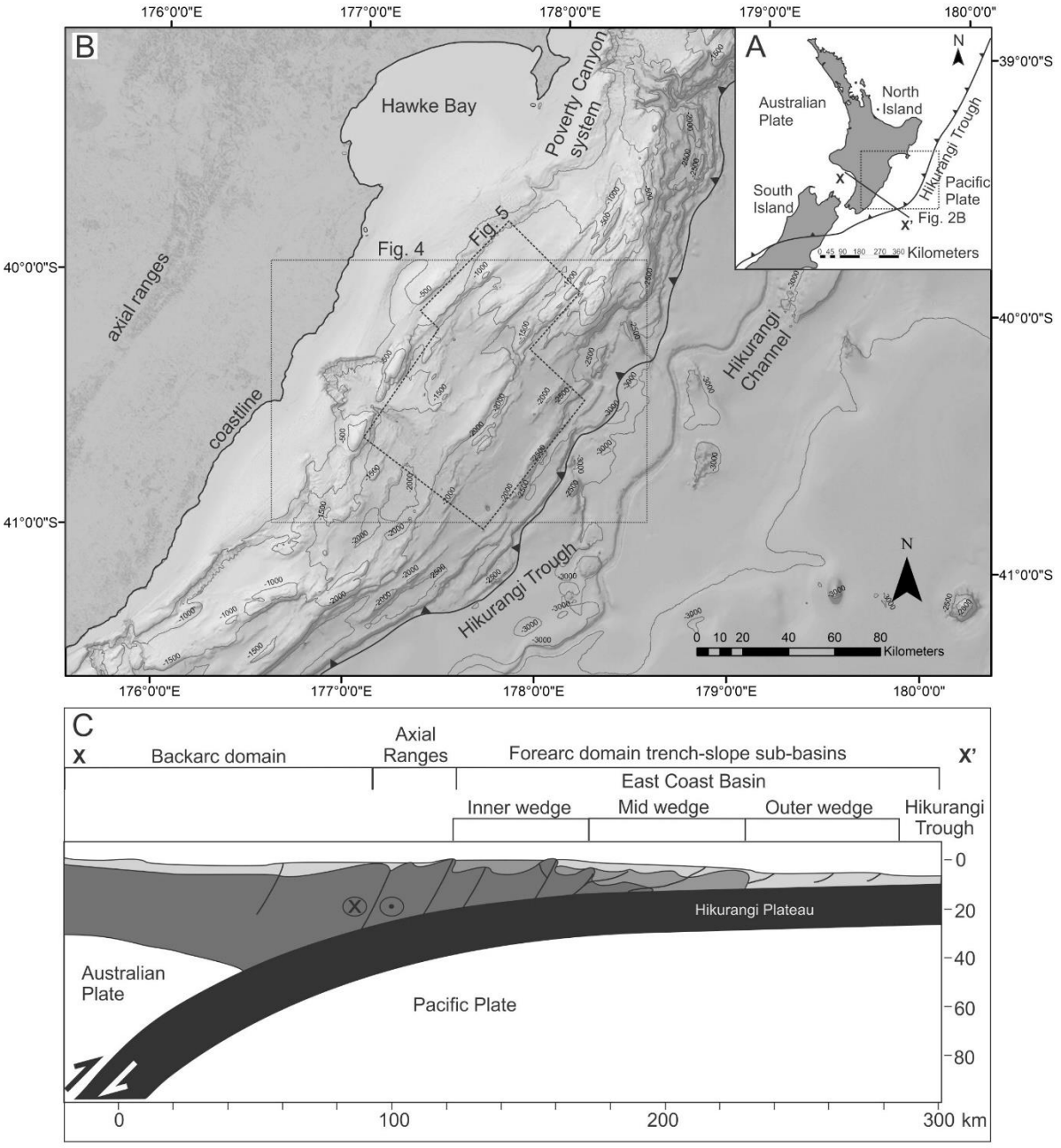

1000

1001 **FIGURE 3**

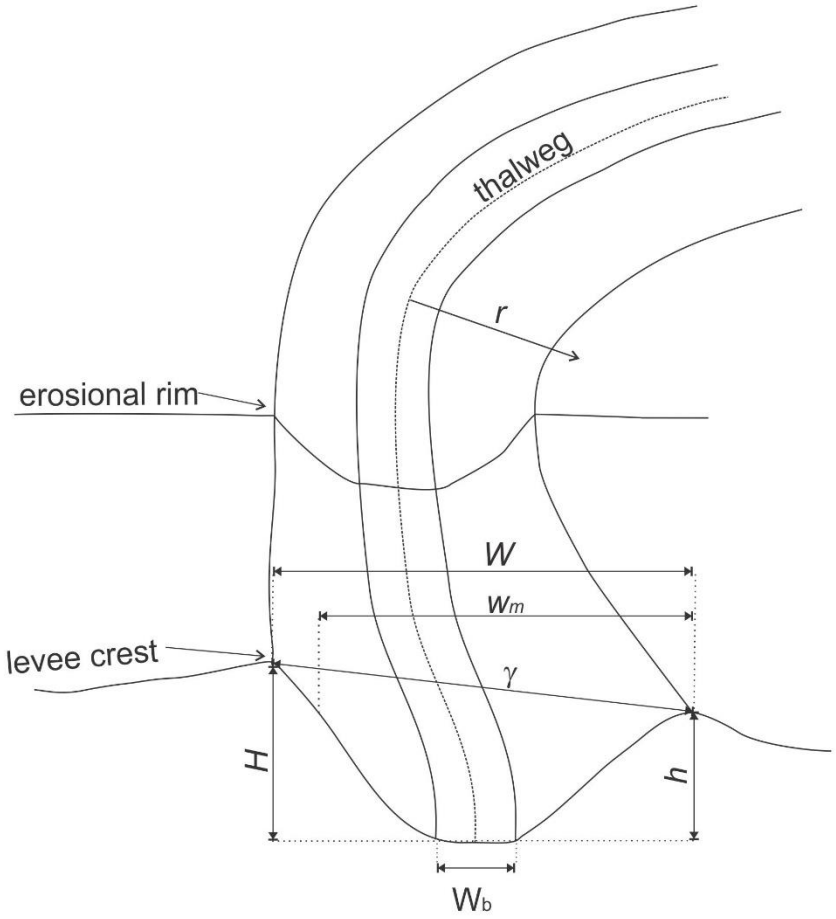

1002

1003 **FIGURE 4**

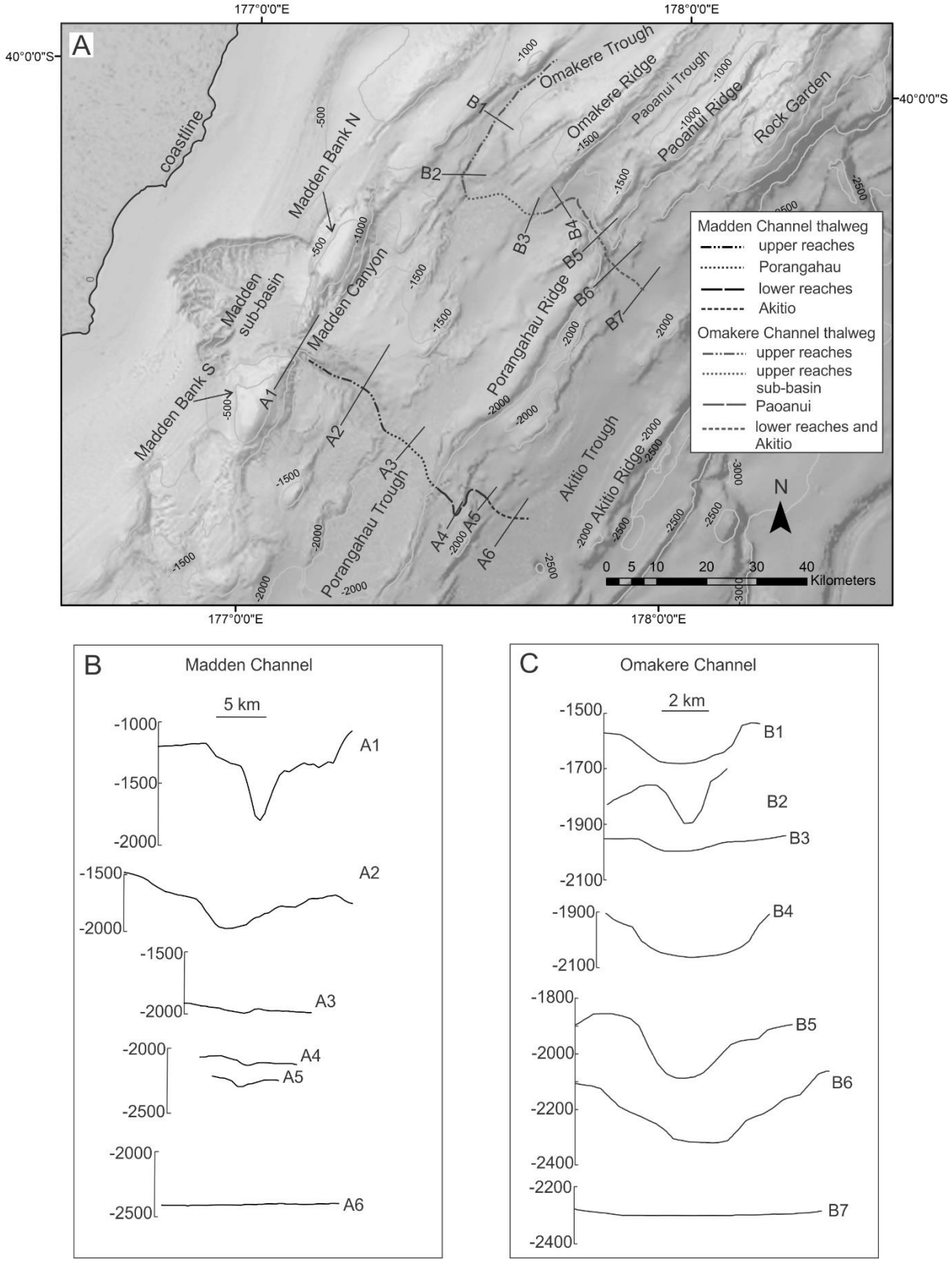

1004

1005 **FIGURE 5**

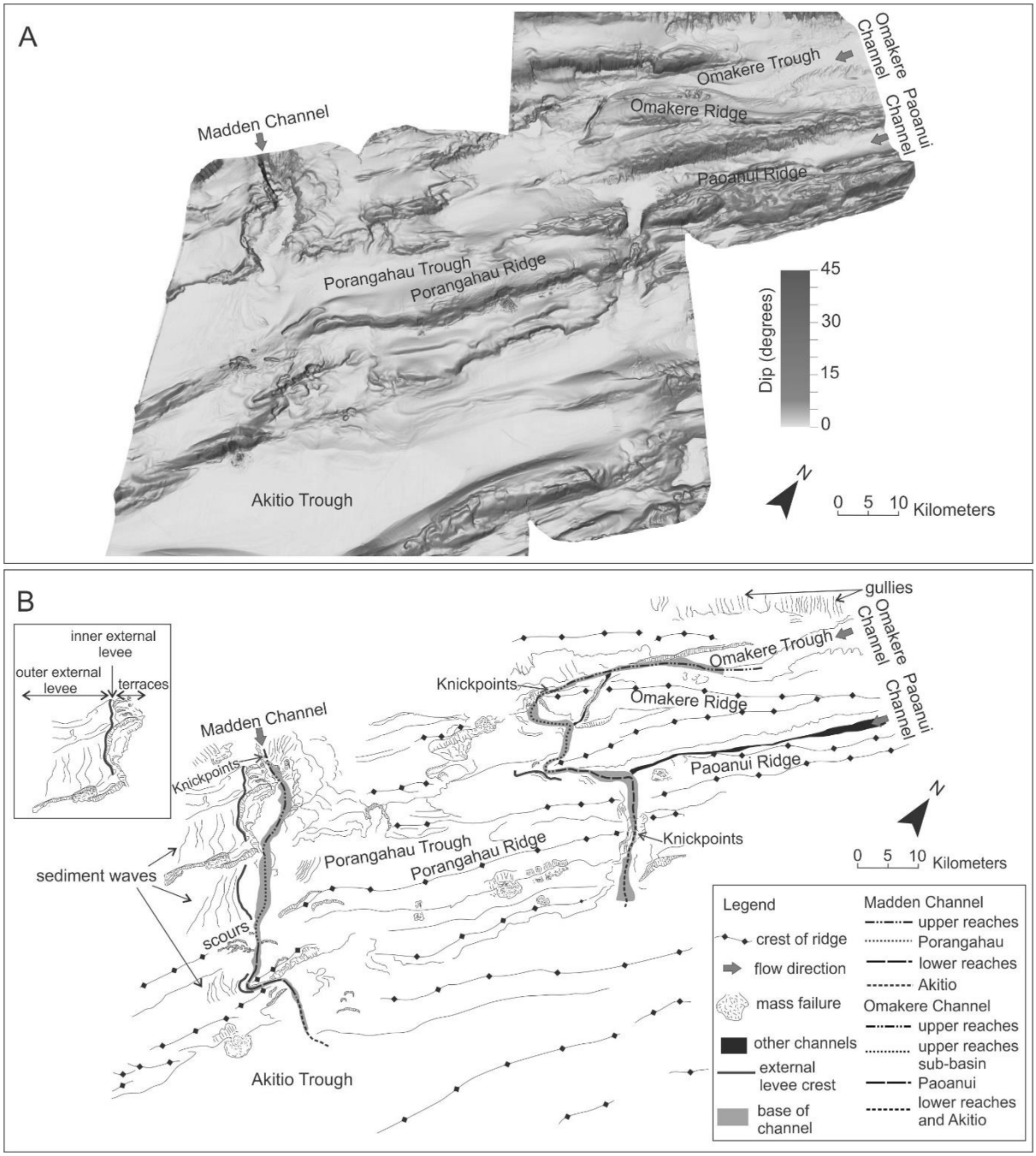

1006

1007 **FIGURE 6**

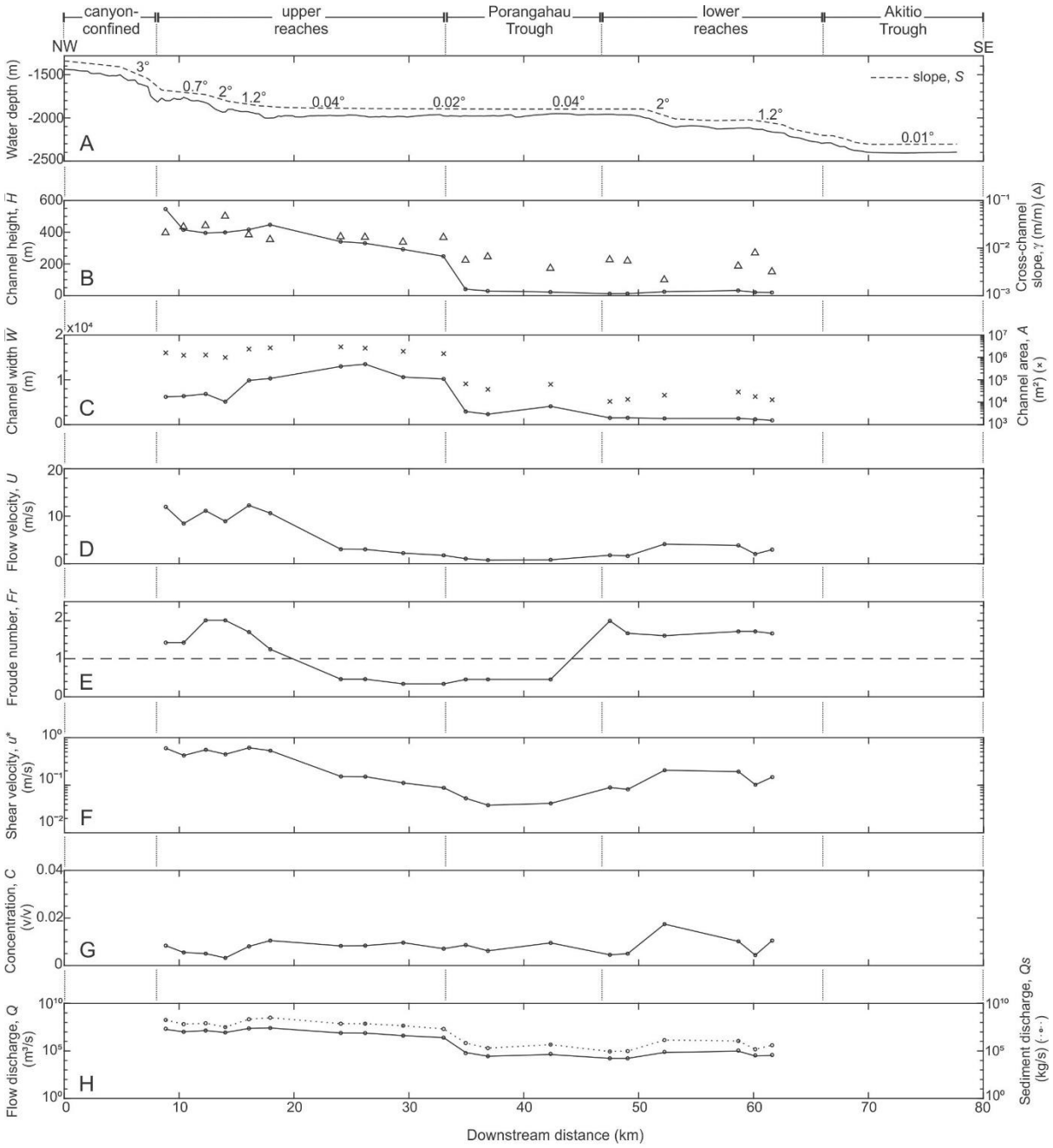

1008

1009 **FIGURE 7**

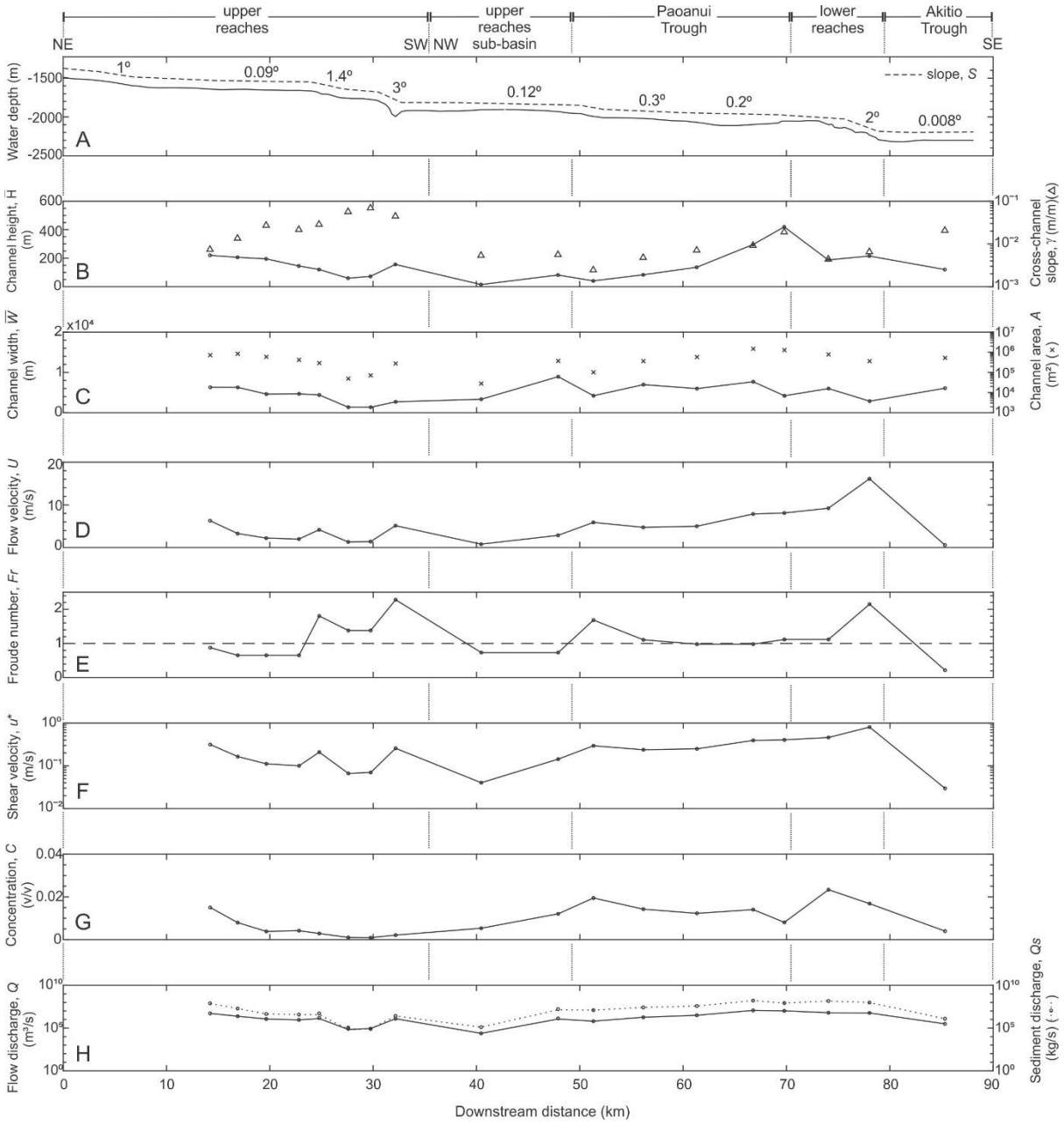

1010

1011 **FIGURE 8**

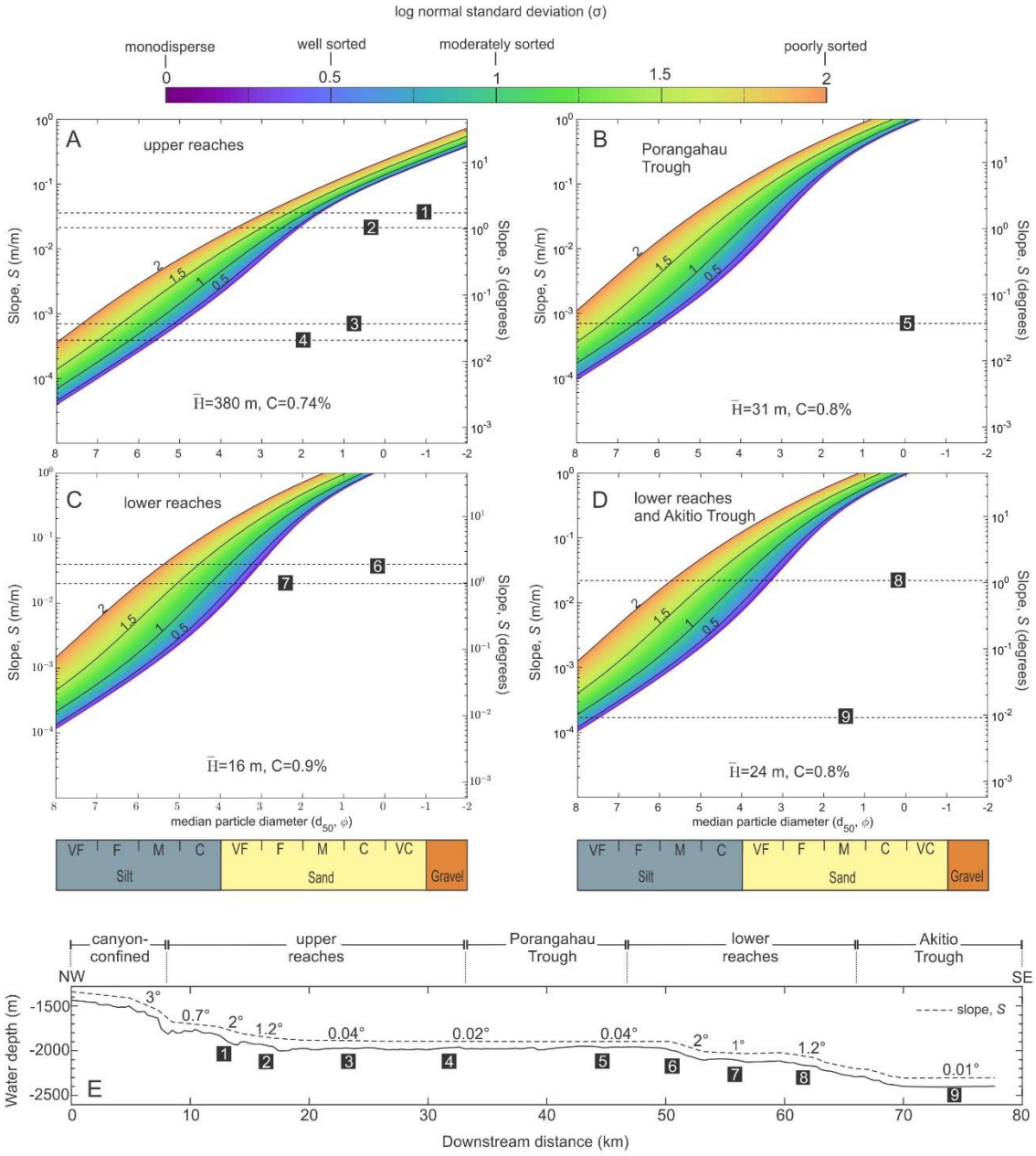

1012

1013 **FIGURE 9**

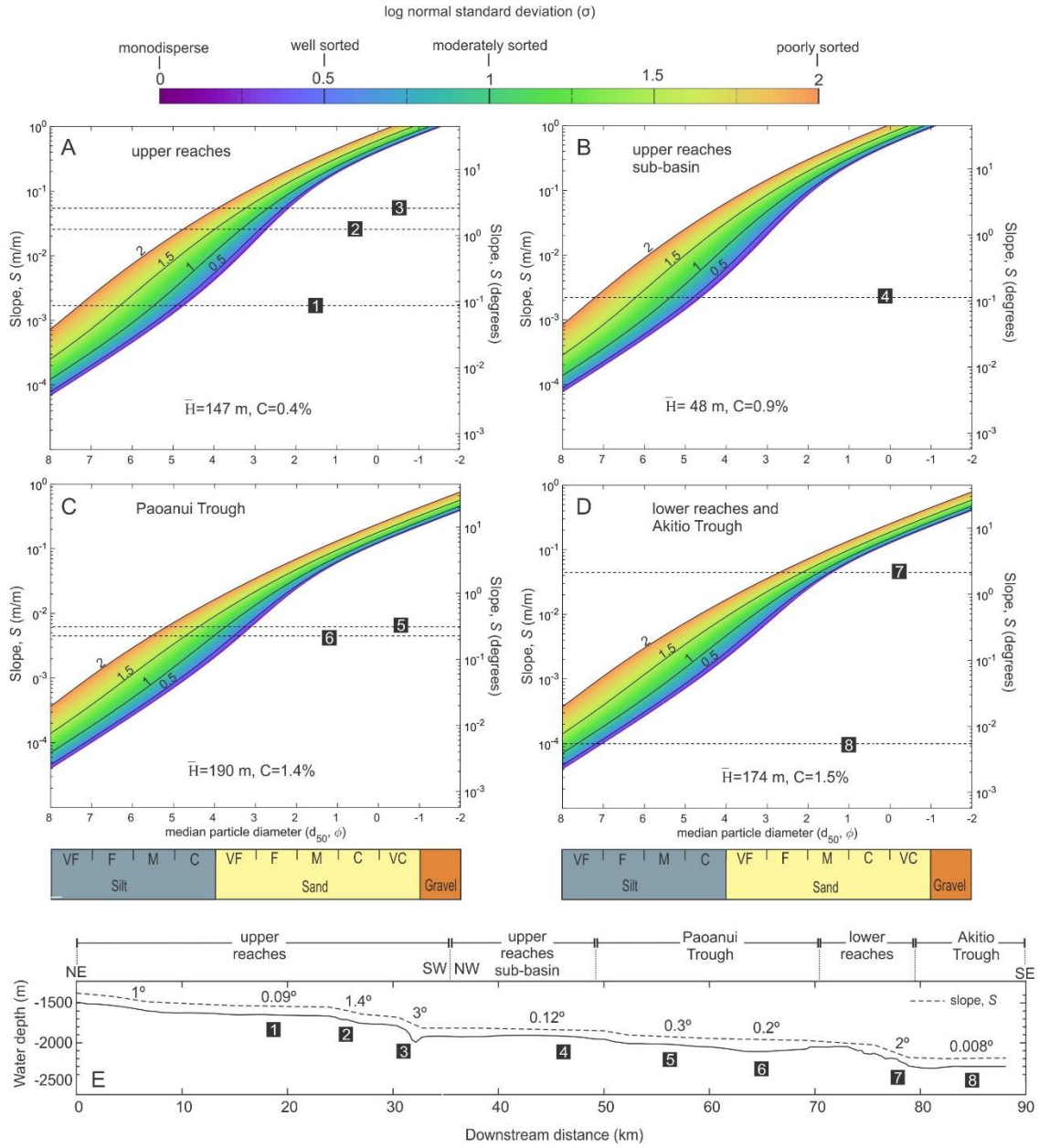

1014

1015 **FIGURE 10**

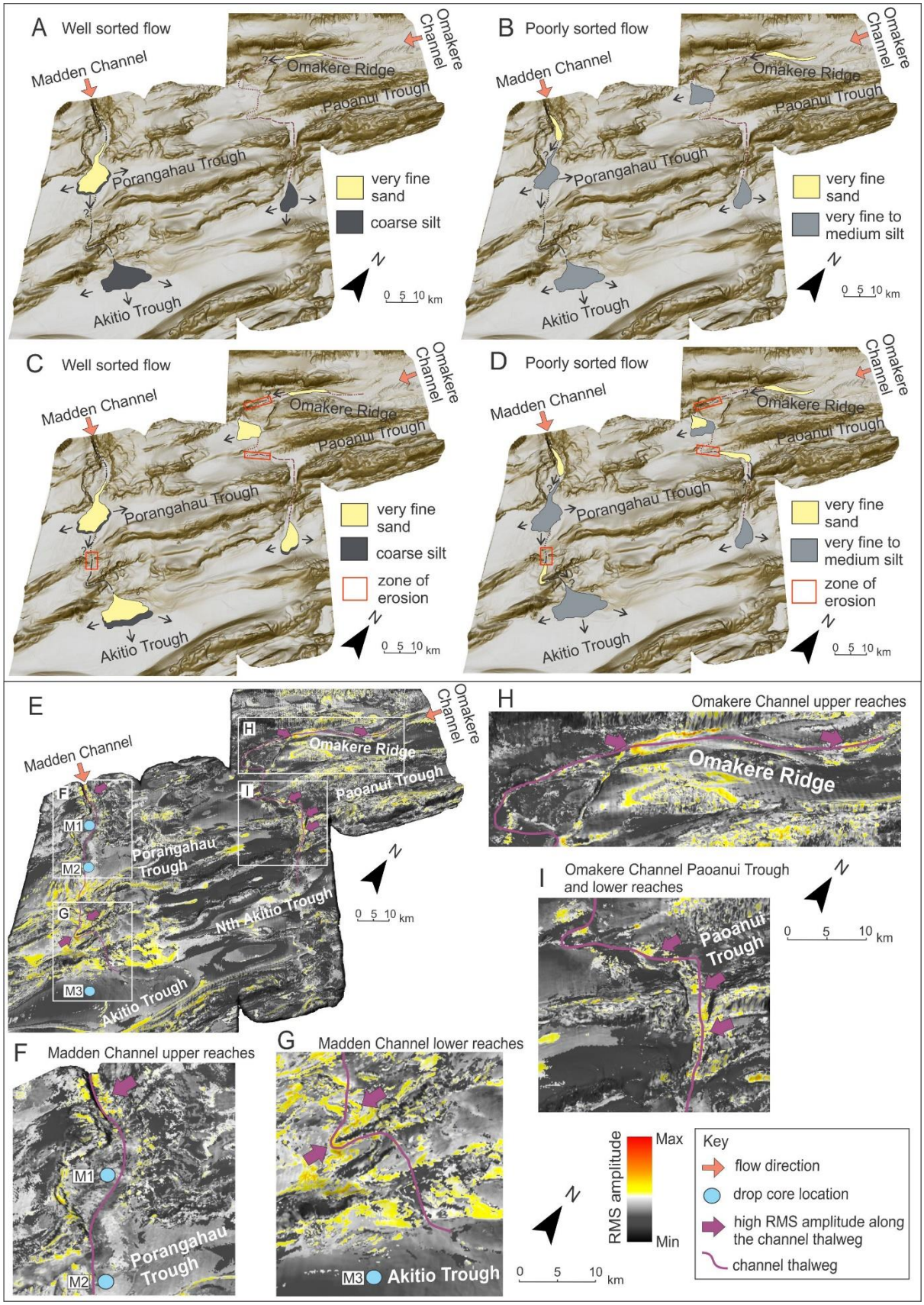
A Well sorted flow
Madden Channel
Omakere Channel
Omakere Ridge
Paoanui Trough
Porangahau Trough
Akitio Trough
very fine sand
coarse silt
0 5 10 km
B Poorly sorted flow
very fine sand
very fine to medium silt
C Well sorted flow
zone of erosion
D Poorly sorted flow
E
F
G
H
I
M1
M2
M3
Nth Akitio Trough
Omakere Channel upper reaches
Omakere Channel Paoanui Trough and lower reaches
Madden Channel upper reaches
Madden Channel lower reaches
RMS amplitude
Max
Min
Key
flow direction
drop core location
high RMS amplitude along the channel thalweg
channel thalweg

1016